Correlating MOF-808 parameters with mixed-matrix membrane (MMM) CO_2 permeation for a more rational MMM development

Raymond Thür[a], Daan Van Havere[a], Niels Van Velthoven[a], Simon Smolders[a], Aran Lamaire[b], Jelle Wieme[b], Veronique Van Speybroeck[b], Dirk De Vos[a], Ivo F.J. Vankelecom[a]

[a]Centre for Membrane Separations, Adsorption, Catalysis and Spectroscopy for Sustainable Solutions (cMACS), KU Leuven, Celestijnenlaan 200F, Box 2454, 3001 Heverlee, Belgium

[b]Center for Molecular Modeling, Ghent University, Tech Lane Ghent Science, Park Campus A, Technologiepark 46, 9052 Zwijnaarde, Belgium

E-mail: ivo.vankelecom@kuleuven.be

Keywords: mixed-matrix membranes; CO_2 adsorption enthalpy; metal-organic framework; parameter correlation; structure-performance; molecular modeling

Abstract

Consistent structure-performance relationships for the design of MOF (metal-organic framework)-based mixed-matrix membranes (MMMs) for gas separation are currently scarce in MMM literature. An important step in establishing such relationships could be to correlate intrinsic MOF parameters, such as CO_2 uptake and the CO_2 adsorption enthalpy (Q_{st}), with the separation performance indicators of the MMM (i.e. separation factor and permeability). Such a study presumes the availability of a platform MOF, which allows systematic comparison of the relevant MOF parameters. MOF-808 can take up the role of such platform MOF, owing to its unique cluster coordination and subsequent ease of introducing additional functional molecules. For this purpose, formic acid (FA) modulated MOF-808 (MOF-FA) was post-synthetically functionalized with five different ligands (histidine (His), benzoic acid (BA), glycolic acid (GA), lithium sulfate (Li_2SO_4) and trifluoroacetic acid (TFA)) to create a series of isostructural MOFs with varying affinity/diffusivity properties but as constant as possible remaining properties (e.g. particles size distribution). CO_2 uptake and CO_2 adsorption enthalpy of the MOFs were determined with CO_2 sorption experiments and Clausius-Clapeyron analysis. These MOF properties were subsequently linked to the CO_2/N_2 separation factor and CO_2 permeability of the corresponding MMM. Unlike what is often assumed in literature, MOF-808 CO_2 uptake proved to be a poor indicator for MMM performance. In contrast, a strong correlation was observed between Q_{st} at high CO_2 loadings on one hand and CO_2 permeability under varying feed conditions on the other hand. Furthermore, correlation coefficients of $Q_{st,15}$ and $Q_{st,30}$ (Q_{st} at 15 and 30 cm^3 (STP)/g) with the separation factor were significantly better than those calculated for CO_2 uptake. The surprising lack of correlation between membrane performance and CO_2 uptake and the strong correlation with Q_{st} opens possibilities to rationally design MMMs and stresses the need for more fundamental research focused on finding consistent relationships between filler properties and the final membrane performance.

1 Introduction

Mixed-matrix membranes (MMMs) consist of a continuous polymer matrix containing dispersed nanoparticles (so-called fillers)[1,2]. While polymeric membranes show good processability but rather moderate gas separation performance[3,4], purely inorganic membranes can reach high selectivity/permeance combinations due to their particular size sieving abilities or strong affinity for the target component[5]. However, inorganic membranes are often uneconomical to produce as they are brittle, making it challenging to prepare up-scaled membranes with large specific surface[6]. MMMs are believed to profit from the best of both worlds, having improved separation capacity due to nanoparticle addition while maintaining the good film-forming properties of the polymer. Much research has been dedicated in the past 10 years to find better combinations of polymers and MOFs with enhanced performance compared to the state-of-the-art[2,7–13]. A lot of these literature reports focus on the use and modification of conventional MOFs, frequently employing a trial-and-error approach for developing novel MMMs. Although the membrane performance can indeed often be boosted by incorporation of MOFs in terms of higher permeability or gas pair selectivity, the theoretical understanding behind the MMM concept remains rather poor and consistent structure-performance relationships for the design of MMMs are currently very scarce[14,15]. A first step towards finding such structure-performance relationships could be the linking of intrinsic MOF parameters to the gas permeation behavior of the MMM (thus determining indicators for the MMM separation performance based on MOF parameters). For example, Seoane and co-workers proposed a method to quantify polymer-MOF compatibility based on the Hansen solubility parameters of MOF and polymer[1]. With respect to the membrane selectivity and permeability, MOF parameters such as pore volume and CO_2 uptake are often identified as key drivers in the ultimate MMM performance, where good MMM separation performance goes hand in hand with high pore volume and CO_2 uptake[16–21]. However, no study has been devoted so far to the systematic correlation between MOF and MMM parameters for a series of isostructural MOFs. This is understandable since such a study presumes the availability of a platform MOF, which allows systematic comparison of the relevant MOF parameters. Furthermore, the overall gas permeation through the MMM is the result of a subtle interplay between polymer and MOF-related factors, which complicates the identification of one-on-one correlations and causalities between parameters.

MOF-808, consisting of the same $Zr_6O_4(OH)_4$ cluster as UiO-66 but linked through six 1,3,5-benzenetricarboxylate (BTC^{3-}) linkers, can take up the role of such a platform MOF since it can be simply modified to change intrinsic MOF properties while preserving the same MOF structure and topology[10]. Next to the six BTC^{3-} linkers occupying the binding sites (at opposing vertices of the cluster), the six equatorial binding sites can theoretically be occupied by up to six modulator or ligand molecules[22] (Figure 1), which can be easily attached via solvent-assisted ligand exchange[23]. As shown in previous work, it is possible to create isostructural MOF-808 derivatives with subtly altered BET surface area, pore volume, CO_2 uptake and CO_2 affinity[10]. Moreover, other appealing features of MOF-808 include its excellent thermal, chemical and mechanical stability, following from the strong interaction of the Zr_6-cluster and the carboxylate ligands, and the easy up-scaling of the synthesis in non-toxic solvents such as water[24].

In this work, post-synthetic functionalization of MOF-808 was applied to create a series of isostructural MOF-808 with systematically varying characteristics, such as pore volume, surface area, CO_2 uptake and CO_2 adsorption enthalpy (Q_{st}). For this purpose, a single batch of MOF-FA was produced to guarantee a uniform starting material for all functionalizations, hence avoiding differences in MOF morphology or particle size due to batch variations. Five different functional molecules (histidine (His), benzoic acid (BA), glycolic acid (GA), lithium sulfate (Li_2SO_4) and trifluoroacetic acid (TFA)) were selected based on their anticipated interaction with CO_2. The polyimide Matrimid 5218 (Matrimid) was used as polymer matrix as it is regarded as a benchmark polymer for membrane gas separation tests in academic research[1,25–27]. The obtained MOF characteristics were correlated with the MMM performance parameters (CO_2/N_2 separation factor, pure gas permeability (PGP) and mixed-gas permeability) in an attempt to identify the MOF parameters that are best suited to use as predictors for the MMM permeation behavior.

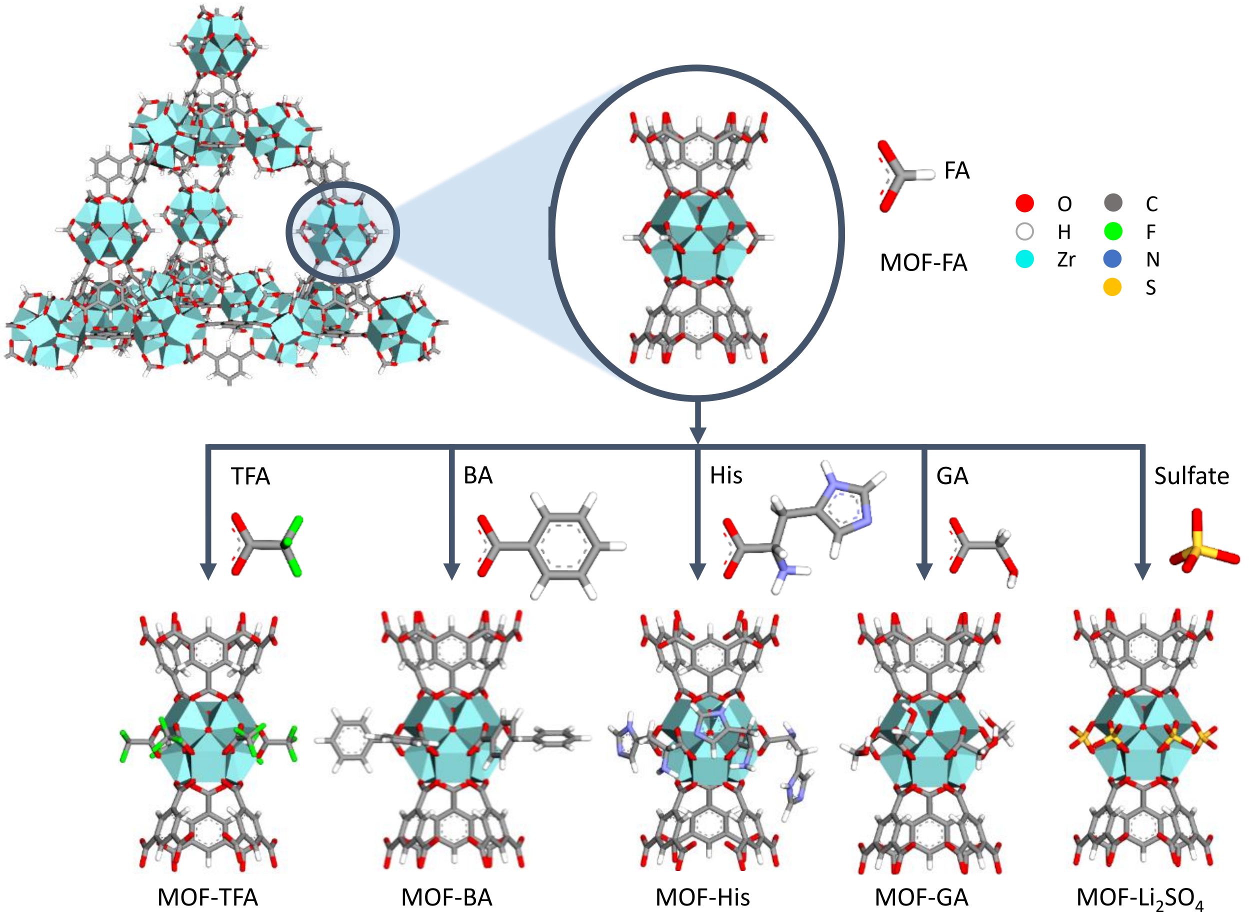

Figure 1: Overview of MOF-808 functionalization strategy. FA = formic acid, TFA = trifluoroacetic acid, BA = benzoic acid, His = histidine, GA = glycolic acid. For clarity, lithium ions are not shown.

2 Experimental and methodology section

2.1 Chemicals

Polyimide (Matrimid 5218) was kindly provided by Huntsman (Switzerland). Sulfuric acid (99.9%), $Li_2SO_4.H_2O$ (>98.5%), BA (>99.5%), GA (99%) and histidine (L, >99%) were purchased from Sigma-Aldrich. TFA (99%) was acquired from Merck-Schuchardt. FA (99%), tetrahydrofuran (THF, >99%), dimethylsulfoxide (DMSO, 99%) acetone (technical grade) and ethanol (pure) were supplied by Acros. Zirconylchloride octahydrate ($ZrOCl_2.8H_2O$) was acquired from Abcr GmbH and BTC from J&K Chemicals. CO_2 (>99.999%) and N_2 (>99.999%) were purchased from Air Liquide and used as delivered.

2.2 MOF synthesis

The different MOF-808 samples are denoted as MOF-*x*, with x being the ligand type, e.g. MOF-808 functionalized with BA is denoted as MOF-BA. A single batch of MOF-FA was prepared (yield 12.6 g) to prevent differences between samples due to batch variations. All functionalized MOFs were synthesized using MOF-FA as starting material.

2.2.1 Synthesis of MOF-FA

The MOF synthesis recipe used in previous work[10] was adapted for using FA as modulator and subsequently scaled up. 5.08 g (24.2 mmol) BTC and 23.4 g (72.8 mmol) $ZrOCl_2.8H_2O$ were dissolved in 182 mL H_2O in a 500 mL round-bottom flask. Subsequently, 26.8 mL FA (712 mmol) was added and the mixture was thoroughly stirred for 15 min. The reaction mixture was then heated to 100 °C under reflux for 5 h in an oil bath. The formed MOF sludge was transferred into Falcon tubes and washed with distilled water (30 mL). After 8 h, the MOF samples were centrifuged (4000 rpm, 30 min) and the supernatant was decanted. This was repeated 4 times with distilled water and 3 times with ethanol. After the last washing step, a clean, white powder (12.6 g) was obtained by drying in a vacuum oven at 70 °C overnight.

2.2.2 Synthesis of MOF-BA

MOF-BA was functionalized according to the method developed by Baek *et al.*[28]. 250 mg of MOF-FA was suspended in a 50 mL DMSO solution with 1.12 g (9.251 mmol) BA in a 100 mL Schott bottle. The bottle was then placed in an oil bath at 100 °C under constant stirring. After 24 h, the reaction was stopped and the reaction mixture poured into Falcon tubes and washed with DMSO (3 times, 30 mL) and acetone (3 times, 30 mL), similar to the washing procedure of MOF-FA. After washing, the MOF was dried at 70 °C and stored for further use.

2.2.3 Synthesis of MOF-His, MOF-TFA and MOF-GA

MOF-FA (250 mg) was suspended in a 50 mL aqueous solution of 0.005 mol ligand (0.78 g histidine, 0.57 g TFA, 0.38 g GA) in a 100 mL Schott bottle. The bottle was placed on a stirring plate for 24 h at room temperature. Afterwards, the functionalized MOFs were washed 3 times with water and 3 times with acetone, similar to the washing procedure of MOF-FA. Finally, the MOFs were dried at 70 °C and stored for further use.

2.2.4 Synthesis of MOF-Li_2SO_4

An aqueous solution of sulfuric acid (0.1 M, 50 mL) was prepared in a 100 mL Schott bottle by mixing 0.268 mL sulfuric acid with 49.732 mL water, in which 250 mg of MOF-FA was suspended to form MOF-SO_4. The mixture was stirred for 24 h at room temperature. Next, MOF-SO_4 was washed with water and acetone, dried and re-suspended in a 50 mL aqueous solution containing 0.64 g (0.005 mol) $Li_2SO_4.H_2O$ for 24 h under continuous stirring. The resulting MOF was washed with water (3 times) and with acetone (3 times), dried at 70 °C and stored for further use.

2.3 Membrane synthesis

The different Matrimid MMMs are denoted as MMM-*x*, with x being the ligand type. For example, the Matrimid MMM containing MOF-TFA is denoted as MMM-TFA.

2.3.1 Preparation of pristine Matrimid membranes

Matrimid membranes were prepared by dissolving 0.42 g of polymer in 5.58 g THF. After stirring overnight, the polymer solution was poured into a Teflon Petri dish (d = 6 cm) in a nitrogen bag. Evaporation of the solvent was slowed down by placing a plastic funnel over the Petri dish. Once the membrane had solidified due to solvent evaporation, the polymer film was removed from the Petri dish and annealed in a muffle oven by heating from room temperature to 110 °C at 5 °C/min. The membrane remained at this temperature for 2 h. Next, the membrane was heated at 5 °C/min to 180 °C for 6 h. Subsequently, the membranes were allowed to cool down naturally.

2.3.2 Mixed-matrix membrane synthesis

10 wt.% MMMs were prepared by dispersing 0.047 g of dried MOF in 5.58 g THF. The dispersion was then thoroughly sonicated for 15 min. Following an adapted priming protocol[20], 0.42 g polymer was added to the dispersion in three steps (0.14 g per turn). All samples were continuously stirred on a magnetic stirring plate. Before and after polymer addition, the samples were sonicated for 15 min. After the final polymer addition, the polymer/MOF dispersion was stirred overnight and cast into a Petri dish (d = 6 cm) in a nitrogen bag. Evaporation of the solvent was slowed down by placing a plastic funnel over the Petri dish. Once the membrane had solidified due to solvent evaporation, the polymer film was removed from the Petri dish and annealed in a muffle oven by heating from room temperature to 110 °C at 5 °C/min. The membrane remained at this temperature for 2 h. Next, the membrane was heated at 5 °C/min to 180 °C for 6 h. The membranes were finally allowed to cool down naturally. Filler loading was determined with the following equation:

$$filler\ loading\ (wt.\%) = 100 \times \left(\frac{m_{filler}}{m_{filler} + m_{polymer}}\right) \qquad (1)$$

with m_{filler} and $m_{polymer}$ the weight of the filler and polymer, respectively.

2.4 Characterization

2.4.1 *X-ray diffraction*

MOF crystallinity was analyzed with X-ray diffraction (XRD). XRD diffractograms were measured by a Malvern PANanlytical Empyrean diffractometer in transmission mode over a 1.3 – 45° 2θ range. A PIXcel3D solid-state detector and Cu anode (Cu Kα1: 1.5406 Å; Cu Kα2: 1.5444 Å) were used for detection and X-ray generation.

2.4.2 *Nuclear magnetic resonance*

Proton and fluorine nuclear magnetic resonance (^{1}H and ^{19}F NMR) measurements were carried out to determine the average number of functionalizer molecules per Zr_6 cluster. First, 3 mg MOF-808 was dispersed in 600 µL deuterated DMSO. Next, 25 µL of a 40 wt.% hydrofluoric acid (HF) solution was added for MOF digestion. For ^{19}F NMR, 10 µL fluorobenzene was added to the mixture as an internal standard. NMR spectra were recorded on a Bruker AMX-300 spectrometer at 300 MHz for ^{1}H NMR and at 400 MHz for ^{19}F NMR (16 scans). A recycle delay time of 30 s was applied for ^{19}F NMR. The output was analyzed with SpinWorks 4.2 software.

2.4.3 *Scanning electron microscopy*

Particle morphology was examined with scanning electron microscopy (SEM, Philips XL30 FEG). To avoid sample charging, all samples were coated with a layer of gold/palladium. Particle size distribution was analyzed with ImageJ and statistical analysis (one-way ANOVA) to determine whether differences in size occurred between the MOFs.

2.4.4 *Attenuated total reflectance – Fourier transform infrared spectroscopy*

Attenuated total reflectance – Fourier transform infrared spectroscopy (ATR-FTIR) measurements on MOF and MMM samples were conducted to identify functional groups. All samples were dried prior to the measurement. A Varian 670 FTIR imaging spectrometer was used, containing a diamond ATR crystal and a Single Point MCT detector. 32 scans were recorded at a resolution of 2 cm^{-1}.

2.4.5 *N_2 and CO_2 physisorption*

N_2 and CO_2 physisorption experiments were performed with a Micromeritics 3Flex surface analyzer. Prior to the measurement, all MOFs were activated under vacuum at 100 °C for 16 h. N_2 physisorption was conducted at -196 °C. Surface areas were calculated via the multi-point BET method applied to the isotherm adsorption branch, taking into account surface area criteria as given by Rouquerol[29] and the consistency criteria described by Walton and Snurr[30]. CO_2 sorption was measured at three different temperatures (273 K, 293 K, 313 K) to allow determination of the CO_2 Q_{st} of the different MOFs with the Clausius-Clapeyron equation (Equation 2)[31]:

$$\frac{\partial\, ln(p)}{\partial\, (\frac{1}{T})} = \frac{-Q_{st}}{R} \tag{2}$$

with p the equilibrium pressure (mbar), T the temperature (K), R the universal gas constant (J/mol K).

The sorption data were first fitted with the dual-site Langmuir model (Equation 3)[31]:

$$N = N_{m,A} \times \frac{b_A \times p}{1 + b_A \times p} + N_{m,B} \times \frac{b_B \times p}{1 + b_B \times p} \tag{3}$$

with N the amount of adsorbed gas (cm^3 (STP)/g), $N_{m,A}$ and $N_{m,B}$ the amount of adsorbed gas at saturation for sorption site A and B respectively (cm^3 (STP)/g), b_A and b_B the adsorption equilibrium constants for respectively sorption site A and B and p the pressure (mbar).

The Clausius-Clapeyron data points were then interpolated based on the fit values. Next, for a range of different CO_2 loadings, Q_{st} can be calculated from the slope of a ln(p) vs 1/T plot, according to Equation 2.

2.4.6 Membrane gas sorption

Sorption of N_2 and CO_2 was measured at 30 °C up to pressures of 15 bar for all membranes. A Rubotherm series IsoSORP© instrument was used to conduct the measurements. First, helium pycnometry was carried out on all membranes to determine the membrane weight and volume. The additional weight resulting from gas sorption in the membrane over time was determined with a magnetically suspended balance. The buoyancy of the measurement gases was taken into account to calculate the correct weight of the sample (Equation 4):

$$m_{corrected} = m_{measured} + \rho_{gas} \times V_{sample} \tag{4}$$

with $m_{corrected}$ the corrected weight (g), $m_{measured}$ the measured weight (g), ρ_{gas} the measuring gas density (g/cm^3) and V_{sample} the sample volume (cm^3).

The N_2 and CO_2 solubility in the membranes can be calculated with Equation 5:

$$S = \frac{C}{p} \tag{5}$$

with S the gas solubility (cm^3(STP)/cm^3cmHg), C the quantity of adsorbed gas (cm^3(STP)/cm^3) and p the pressure (cmHg).

2.4.7 Grand Canonical Monte Carlo (GCMC) simulation of CO_2 adsorption behavior in MOF-808

The input structures for the GCMC simulations were obtained by optimizing the primitive unit cell of the different MOF-808 structures using CP2K[32]. The optimizations were performed at the PBE-D3(BJ)[33–35] level of theory, combined with Gaussian TZVP-MOLOPT[36] basis sets, a plane wave basis set with a cut-off of 800 Ry and a relative cut-off of 60 Ry, and Goedecker-Teter-Hutter (GTH) pseudopotentials[37], allowing for a relaxation of both the atomic positions and the unit cell. The GCMC simulations were performed with RASPA[38], using a fixed framework and rigid CO_2 and N_2 adsorbate molecules described by the TraPPE force field[39]. The atomic framework charges were derived from cluster calculations using the Minimal Basis Iterative Stockholder (MBIS) partitioning scheme[40] (see Supporting Information for more details), while the Lennard-Jones interaction parameters are taken from the DREIDING model[41] (except for zirconium, which was taken from UFF[42,43]. The temperature was set to 300 K. Each GCMC simulation consists of 10^7 cycles, with equal probabilities for translation, rotation, and (re)insertion moves. The first 10^5 cycles are regarded as equilibration steps and are not taken into account in any analysis.

The CO_2 enthalpy of adsorption can be determined from the GCMC simulations using Equation 6:

$$\Delta H_{ads} = \frac{\langle U \cdot N \rangle_\mu - \langle U \rangle_\mu \langle N \rangle_\mu}{\langle N^2 \rangle_\mu - \langle N \rangle_\mu^2} - \langle U_{host} \rangle - \langle U_{guest} \rangle - k_B T \tag{6}$$

with U the total energy of the host framework and the adsorbed molecules, N the number of adsorbed molecules, $\langle U_{host} \rangle$ the average energy of the adsorbent, $\langle U_{guest} \rangle$ the average energy of the adsorbate molecule in the gas phase, k_B the Boltzmann constant, and T the absolute temperature.

$\langle \dots \rangle_\mu$ denotes an average in the grand-canonical ensemble. As the host framework and the adsorbed molecules are described as rigid molecular systems, $\langle U_{host} \rangle = \langle U_{guest} \rangle = 0$.

The mixed-gas CO_2/N_2 selectivities of MOF-FA and MOF-TFA were determined from a separate set of GCMC simulations in which both CO_2 and N_2 molecules can be inserted or deleted. The mole fractions were set to 0.5, so that the selectivity can be calculated from the ratio of the number of adsorbed CO_2 molecules to the number of adsorbed N_2 molecules.

2.4.8 Gas permeation

Our in-house developed high-throughput gas separation set-up (HTGS) was used to examine the gas permeation behavior of the synthesized membranes. A detailed set-up description is given elsewhere[44–46]. HTGS allows simultaneous pure gas and mixed-gas testing of 16 membrane coupons at varying membrane temperatures and feed pressures. The active membrane area is 1.91 cm^2. CO_2 pure gas permeability and the CO_2/N_2 mixed-gas permeability and separation factor were measured for all membranes.

CO_2/N_2 mixed-gas separation factors (α^*) were measured by a GC analysis of the permeate composition. The ratio of the feed and permeate mole fraction of CO_2 and N_2 then renders the separation factor (Equation 7):

$$\alpha^*_{CO2/N2} = \frac{y_{CO2} / y_{N2}}{x_{CO2} / x_{N2}} \qquad (7)$$

where y_{CO2} and y_{N2} are the mole fractions of CO_2 and N_2 in the permeate, x_{CO2} and x_{N2} the mole fractions of gas CO_2 and N_2 in the feed. The ratio y_{CO2}/y_{N2} is determined from chromatogram peak areas of the permeate, while x_{CO2}/x_{N2} is determined by the feed settings.

Determination of the pure gas and mixed-gas permeabilities of CO_2 and N_2 was performed with a constant-volume-varying-pressure method. A pressure sensor (MKS Baratron) measures the change in pressure in a 75 cm^3 measuring cylinder while permeate gas is accumulated in the cylinder. The change in pressure as a function of time (dp/dt) is then used to calculated the permeability P (Barrer) with Equation 8. For pure gas measurements, the mole fraction of the gas in permeate and feed is 1.

$$P_{CO2} = 10^{10} \times \frac{y_{CO2} \times V \times V_m \times L}{x_{CO2} \times p_{up} \times A \times R \times T} \times \frac{dp}{dt} \qquad (8)$$

with P_i the gas permeability (Barrer), y_i the mole fraction of the component in the permeate, x_i the mole fraction of the component in the feed, V the downstream volume (cm^3), V_m the molar volume (22.414 L/mol), A the membrane permeation area (1.91 cm^2), L the membrane thickness (µm), T the operating temperature (K), p_{up} the upstream pressure (bar), R the gas constant (0.082 L atm/mol K) and dp/dt the pressure increase (Torr/s).

3 Results and discussion

3.1 Characterization of MOFs and membranes

Functionalization of the starting material MOF-FA does not change the crystal structure of the MOF since all its functionalized derivatives show a high degree of crystallinity (Figure S1), in good agreement with literature[10,23,28]. The variation in relative intensity between the large diffraction peak at 4.3° and the two smaller peaks at 8.3° and 8.7° can be attributed to the varying pore filling of the different MOFs[47–49]. Furthermore, post-synthetic functionalization does not affect the particle size nor morphology as confirmed by SEM (Figure S2). All MOFs have the same, lumped octahedral shape and a uniform, average MOF size of around 350 nm, originating from the starting material. A one-way analysis of variance (ANOVA) suggested no statistical difference in particle size between the MOFs (Table S1 and Table S2).

ATR-FTIR was used to further confirm the presence of the different ligands in the MOFs (Figure 2). In all spectra, peaks situated at 453 cm^{-1} (Zr-μ$_3$-OH stretch) and 660 cm^{-1} (Zr-μ$_3$-O stretch) are associated with the Zr-oxide cluster[20]. Likewise, clearly distinguishable peaks are observed at 760 cm^{-1}, 1385 cm^{-1}, 1572 cm^{-1} and 1620 cm^{-1}, corresponding to vibrations of the BTC linker[50]. No signal was found between 1715-1750 cm^{-1}, which corresponds with the C=O stretch of uncoordinated ligands or BTC, hence indicating that the MOF pores do not contain physisorbed ligands[50]. Specific peaks belonging to the ligand were found for all samples. Additional bands for MOF-His are visible at 822 cm^{-1} and 1067 cm^{-1}, resulting from mixed $-NH_3^+$ and -CH bending. Together with the higher relative absorbance of the signal at 1574 cm^{-1} ($-NH_3^+$ deformation), these absorptions suggests that histidine is present in its (partially) protonated form[51–53]. Specific absorption bands for MOF-TFA were recorded at 1170 and 1208 cm^{-1}, attributed to -CF symmetrical and anti-symmetrical stretch, respectively[10]. Signals for MOF-BA and MOF-GA were less pronounced as their characteristic bands mostly coincide with linker peaks. For MOF-BA, the signal at 718 cm^{-1} has a higher absorbance (associated with an increased out-of-plane -CH stretching of the benzene ring) while a new peak occurs at 1178 cm^{-1} (-CH bending ring)[54]. MOF-GA shows a weak signal increase at 1000-1075 cm^{-1} (C-O stretch) but, most importantly, a broad signal at 3300 cm^{-1} due to -OH stretch (from GA, ethanol or water)[52]. Finally, an enhanced absorbance intensity in the 900-1200 cm^{-1} region has previously been associated with effective SO$_4$ functionalization of MOF-808[55].

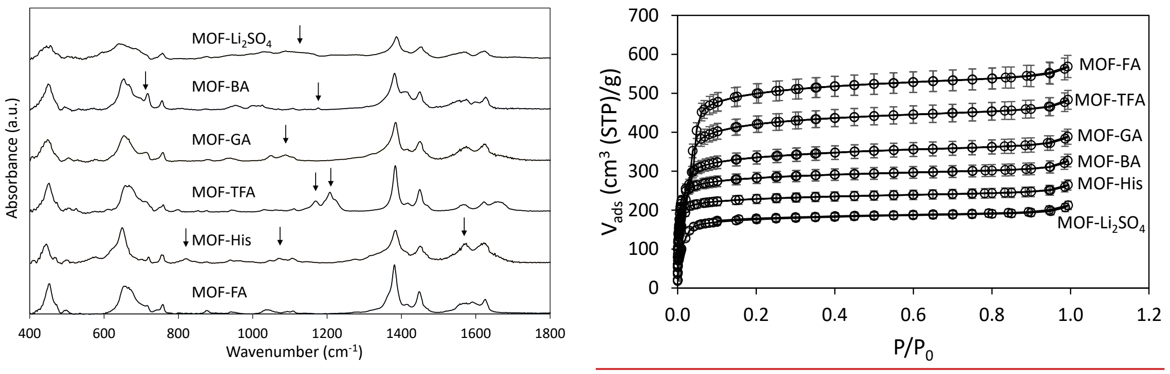

Figure 2: ATR-FTIR spectrum (left) and N_2 adsorption isotherms at 77 K (right) of all MOFs.

Further confirmation of successful post-synthetic functionalization was performed with ^{1}H NMR and ^{19}F NMR (Figure S4). A higher ligand loading on the cluster was detected in the following order: MOF-TFA =

MOF-His (3.3) > MOF-BA (3.2) > MOF-GA (2.3) > MOF-FA (2.2), as can be seen in Table 1. The difference in loading seems to roughly increase with decreasing pK_a of the carboxylic acid functional group (in water): TFA (0.23) > His (1.78) > GA (3.83) ~ FA (3.75)[56,57]. A lower pK_a results in a larger concentration of deprotonated ligand at equal pH and thus a higher probability of incorporation in the MOF framework. MOF-BA deviates from this trend as it has the highest pK_a (4.20) but, at the same time, a loading of 3.2 BA per Zr_6 cluster. Due to the limited solubility of BA in water, BA functionalization took place in DMSO, whereas the other functionalizations were water-based, making it difficult to draw conclusions with regard to BA. None of the functional ligands had a cluster loading equal to the theoretical maximum of six, indicating that the remaining vacant sites were occupied by other charge compensating moieties (i.e. $-OH^-$, $-Cl^-$)[28].

CO_2 and N_2 physisorption experiments were conducted to determine characteristic MOF-808 parameters, such as pore volume and diameter, BET value and CO_2 uptake (Table 1). N_2 adsorption isotherms are given in Figure 2. Substantial differences in BET surface area and pore volume exist between the functionalized MOFs. For the starting material MOF-FA, BET and pore volume correspond well with literature[10,24,58]. The BET surface area, pore volume and pore diameter (Figure S5) all decrease with increasing size of the ligand (MOF-TFA > MOF-GA > MOF-BA > MOF-His). Although Li_2SO_4 is considerably smaller in size than histidine and BA, MOF-Li_2SO_4 denotes the lowest BET and pore volume measured. As MOF-Li_2SO_4 retained its crystalline structure after functionalization, the low BET and pore volume suggest that the MOF pores might be partially blocked by salt deposition.

Furthermore, functionalization strongly affects the CO_2 uptake of the different MOFs as well (Figure S6). At 1000 mbar and 273 K, the MOF-FA starting material displays the highest uptake (65.9 cm^3 (STP)/g), indicating that functionalization reduced the uptake capacity of the MOFs. The CO_2 uptake follows a decreasing trend from MOF-FA > MOF-His > MOF-TFA > MOF-GA > MOF-BA > MOF-Li_2SO_4. However, only small differences in uptake (ranging from 48.1-55.2 cm^3 (STP)/g) are observed between the functionalized MOFs, except for MOF-Li_2SO_4, which loses more than 40% of uptake capacity compared to MOF-FA, further pointing towards the deposition of Li_2SO_4, blocking adsorption sites[59]. Besides the total CO_2 uptake capacity of the MOF, the initial slope of the CO_2 adsorption isotherm in the low-pressure region also reveals qualitative information about the MOF CO_2-philicity as it is governed by the sorption equilibrium constant (b-value)[60–63]. Hence, adsorption in this pressure region is expected to correlate primarily with the MOF-CO_2 binding strength rather than with the specific surface area or pore volume. The slope in the lower pressure region (0-100 mbar, Figure S7) increases in the order MOF-BA < MOF-Li_2SO_4 < MOF-GA <

MOF-FA ≈ MOF-His < MOF-TFA, which was further confirmed by the b-values obtained from the dual-site Langmuir model (Table S3). The observed trends in CO_2 uptake and initial slope (b-value) indicate that MOF-TFA has the highest affinity for CO_2, although this is eventually not reflected in the highest total CO_2 uptake since the MOF starting material (i.e. MOF-FA) can adsorb up to 28% more CO_2. While this observation seems to contradict at first sight, it can be explained by the larger pore volume and surface area of MOF-FA. Furthermore, an almost linear CO_2 adsorption isotherm is observed for MOF-BA in the low-pressure region, which has previously been associated with a lack of high-affinity bindings sites in the MOF[63,64]. At higher pressures, the difference between the isotherms of the other MOFs is less pronounced (Figure S6).

Table 1: Average number of ligand molecules per Zr_6 cluster, pore volume (cm^3), pore diameter (Å), BET value (m^2/g) and CO_2 uptake (cm^3 (STP)/g) at 273 K and 1000 mbar for all MOFs.

	Ligands per Zr_6 cluster[#]	**Pore volume (cm^3)**	**Pore diameter (Å)**	**BET value (m^2/g)**	**CO_2 uptake (cm^3 (STP)/g)[*]**
MOF-FA	2.2	0.76	18.4	2304	65.9
MOF-TFA	3.3	0.68	17.7	1946	51.2
MOF-GA	2.3	0.55	15.6	1421	50.9
MOF-BA	3.2	0.46	13.8	1119	48.1
MOF-His	3.4	0.37	10.9	901	55.2
MOF-Li_2SO_4	-	0.28	15.6	727	37.2

[#]as determined by NMR, [*]at 273 K and 1000 mbar

To obtain a more accurate and quantitative measure of the effect of functionalization on the MOF CO_2 affinity, the loading-dependent CO_2 Q_{st} was calculated for each MOF with the Clausius-Clapeyron method based on a dual-site Langmuir model (Figure 3). Table S4 gives the MOF Q_{st} values at different loadings. At zero coverage, the diverse functionalizations result in a difference of ~15 kJ/mol between the highest Q_{st} (MOF-TFA, 39.2 kJ/mol) and the lowest Q_{st} (MOF-BA, 23.9 kJ/mol). The curve of the graphs of MOF-FA, MOF-TFA, MOF-GA, MOF-Li_2SO_4 and (to a lesser extent) MOF-His all display a substantial Q_{st} reduction with increasing coverage. Comparable behavior has been associated with the saturation of high-affinity gas binding sites inside the MOF[65,66]. The minima in Q_{st} observed for MOF-FA and MOF-Li_2SO_4 are believed to be an artefact of the model's limited number of temperature data points. For the higher coverages, the Q_{st} appears to approach a pseudo-constant value of roughly 21-22 kJ/mol, with only small differences in the adsorption enthalpy between the MOFs, corresponding with the occupation of the low-affinity adsorption sites in the isostructural MOFs[66]. The change in Q_{st} of MOF-BA remains rather limited, suggesting a larger binding site homogeneity (as was also concluded from the CO_2 adsorption isotherm). CO_2 Q_{st} values in this work are comparable to the Q_{st} values reported in literature for similar MOFs. Plonka *et al.* found a Q_{st} of 32 kJ/mol for FA modulated MOF-808, well in line with our findings[67]. Very similar values were reported for perfluoroalkane functionalized NU-1000 (which contains the same Zr_6 cluster as MOF-808) with $Q_{st,0}$ between 20 and 34 kJ/mol while the pristine NU-1000 gave a CO_2 $Q_{st,0}$ of 17 kJ/mol[66,68]. For UiO-66, CO_2 adsorption enthalpies at zero coverage vary between 26 and 38 kJ/mol, depending on the type of functionalization[69,70]. The highest Q_{st} in this work was noted for MOF-TFA over the entire range of CO_2 loading.

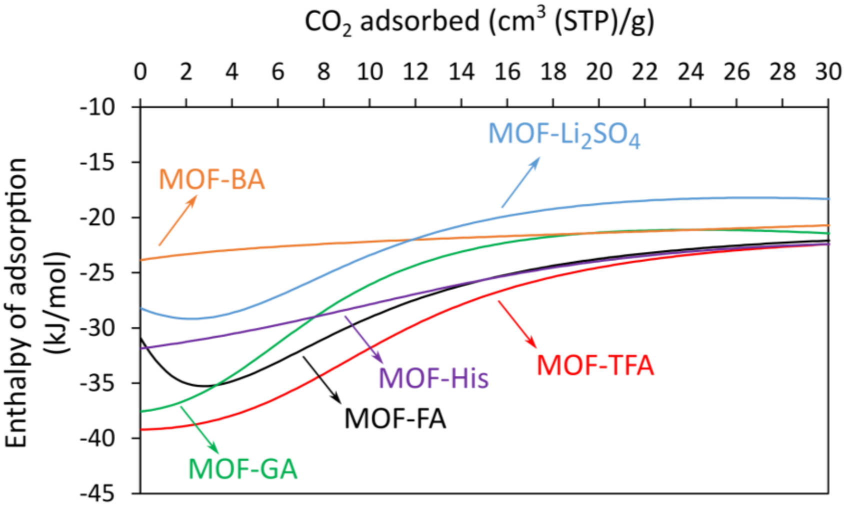

Figure 3: Experimental CO_2 adsorption enthalpies as a function of CO_2 loading for all MOFs.

SEM cross-sections of the MMMs show that the different MOFs are homogeneously incorporated in the polymer matrix, without noticeable differences between the samples (Figure S12 and Figure S13). TGA measurements revealed that thermal stability of the membranes after incorporation of the MOF remained at the same level for all MOFs (Figure S14). In addition, all MMMs contained between 8 and 10 wt.% MOF. An enhanced T_g was observed for all MMMs compared to the unfilled Matrimid membrane (T_g = 312 °C), indicating polymer rigidification at the polymer/particle interphase to a certain extent (Figure S15). Only small variations in T_g can be observed between the MMMs, suggesting a very similar degree of polymer rigidification for the different MMMs. All MMMs have a T_g between 320 and 322 °C with an exception of MMM-FA (T_g = 324 °C). This is most probably a result of the slightly higher weight percentage of MOF-FA in the membrane as can be observed from TGA data. Finally, N_2 and CO_2 sorption were measured for all membranes (Figure 4) and the corresponding solubility values were calculated in Table S5. With increasing pressure, CO_2 sorption in the membranes clearly increases from Matrimid < MMM-

GA < MMM-His < MMM-BA < MMM-FA < MMM-Li_2SO_4 < MMM-TFA. On the other hand, the N_2 sorption data are more difficult to analyze as only small differences between the samples can be noticed. In general, a strong improvement in solubility selectivity is observed for FA, BA, TFA and Li_2SO_4 functionalized MOF-808 compared to the pristine Matrimid membrane while MOF-GA and MOF-His only modestly affect the CO_2/N_2 solubility selectivity. At 5 bar, the highest solubility selectivities are measured for MOF-TFA (17.8) and MOF-Li_2SO_4 (18.4), which represent an 54% and 59% increase compared to Matrimid, respectively.

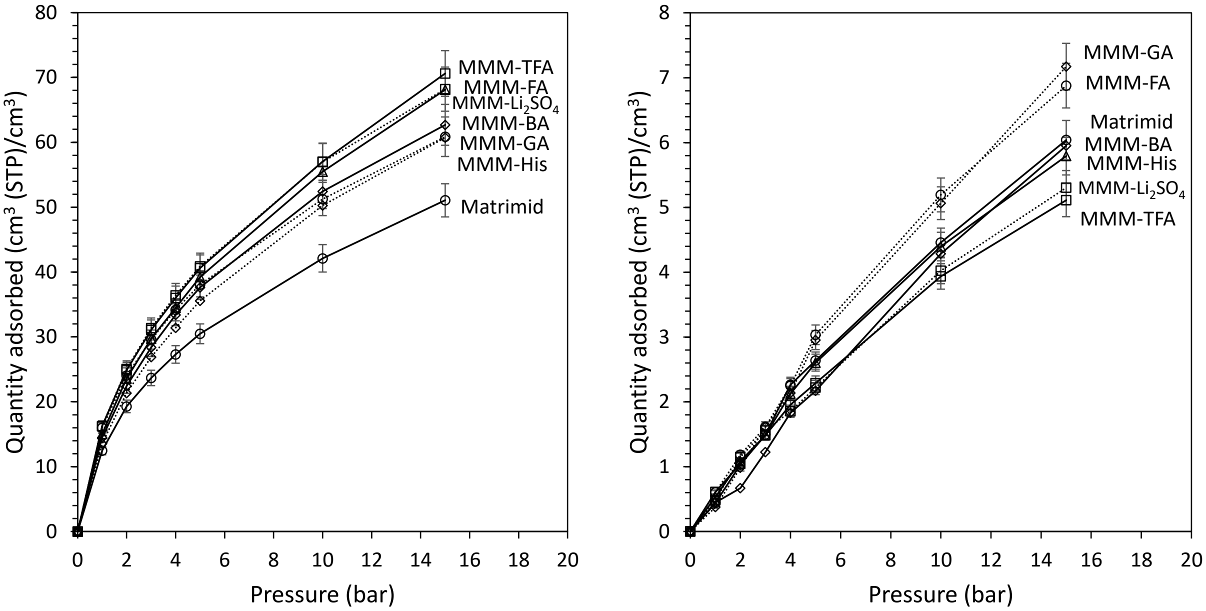

Figure 4: CO_2 (left) and N_2 (right) sorption in the Matrimid reference membrane and all MMMs.

3.2 Computational MOF characterization

GCMC simulations were applied on MOF-FA and MOF-TFA to acquire the MOF CO_2 adsorption sites, adsorption enthalpy and mixed-gas CO_2/N_2 adsorption selectivity. Additionally, the CO_2 adsorption isotherms were simulated and are available in Figure S9.

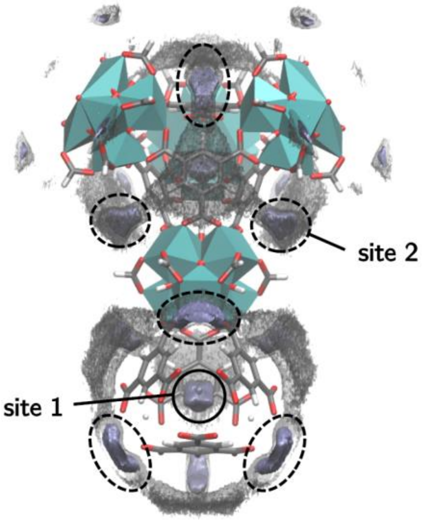

Figure 5: Two isosurfaces of the density of MOF-FA from GCMC simulations at 2 bar. The high density isosurface of sites 1 and 2 is shown in iceblue and a lower density isosurface is shown to encapsulate the metal cluster.

The adsorption densities of the CO_2 molecules at different pressure for MOF-FA are displayed in Figure 6, in which the primitive unit cell was expanded to the conventional cubic cell for ease of interpretation (Figure S10). At low pressures, the CO_2 molecules are primarily located within the cages formed by the four benzene rings of the linker, yielding a square grid of adsorption sites when viewing MOF-808 along the c-axis (marked as site 1 in Figure 5 and Figure 6). A second type of adsorption sites that gain importance with increasing pressure are located in between the zirconium clusters, covering the open sides of the linkers (marked as site 2 in Figure 5 and Figure 6)[67]. At higher pressures, the linkers eventually become fully encapsulated by CO_2 with increasing pressure.

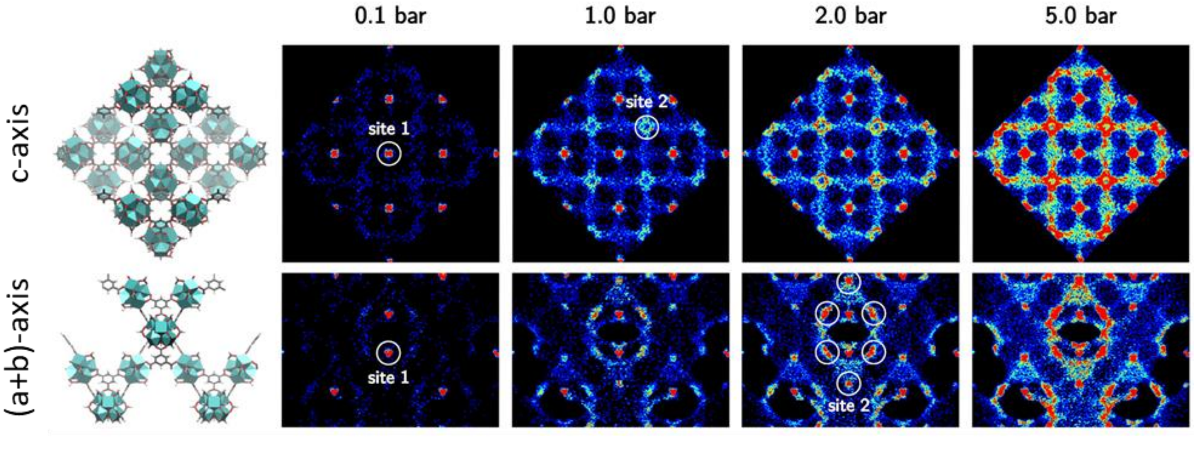

Figure 6: Density of the adsorbed CO_2 molecules in MOF-FA at 300 K projected on a plane orthogonal to the c-axis and the (a+b)-axis of the conventional unit cell. The CO_2 molecules are represented by the positions of the carbon atoms.

Although the adsorption sites for MOF-TFA are similar, the filling pattern is different due to the presence of the TFA functional groups, which results in a higher degree of localization of the adsorbed CO_2 molecules (Figure 7). After filling the tetragonal cages at the lowest pressures, the CO_2 molecules further adsorb onto the linkers. In contrast to MOF-FA, the adsorption sites located above the benzene rings of the linkers are also significantly occupied for mid-range pressures, implying that the surrounding TFA functionalizations enhance the adsorption energy of these sites (more negative adsorption enthalpy).

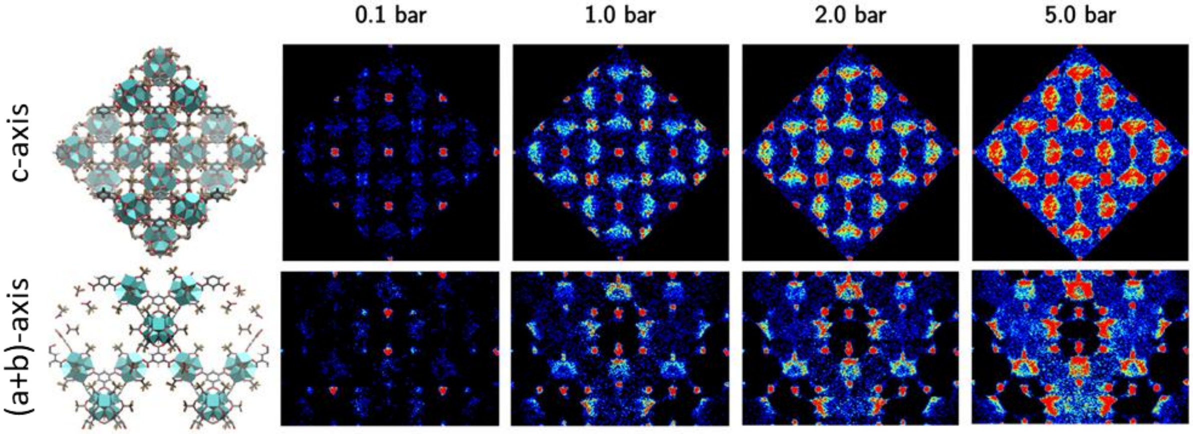

Figure 7: Density of the adsorbed CO_2 molecules in MOF-TFA at 300 K projected on a plane orthogonal to the c-axis and the (a+b)-axis of the conventional unit cell. The CO_2 molecules are represented by the positions of the carbon atoms.

This is also confirmed by the calculated enthalpies of CO_2 adsorption for both MOFs (Figure 8, also Table S6). At the lowest pressures, the enthalpy of adsorption is completely dominated by the host-adsorbate interaction. Initially, the enthalpy values for MOF-FA and MOF-TFA are hence very similar as CO_2 first adsorbs in the tetragonal cages (site 1). Once adsorption sites on the linker molecules (site 2) become relevant, MOF-TFA shows significantly lower adsorption enthalpies (stronger host-adsorbate interaction), in good agreement with the experimentally determined isosteric CO_2 adsorption enthalpy. A more moderate difference is observed at higher pressures as the adsorbate-adsorbate interactions also start to contribute to the adsorption enthalpy. Eventually, this is reflected in higher mixed-gas CO_2/N_2 selectivities for MOF-TFA, confirming the experimental trends. Finally, the influence of open metal site defects (i.e. as a result of missing modulators) on the enthalpy of adsorption was also investigated for MOF-FA, by creation of a MOF-FA structure with 1 defect (MOF-FA-def1) and 3 defects (MOF-FA-def3), respectively (Figure S11 and Table S6). As can be seen in Figure 8, no difference in CO_2 adsorption enthalpy is observed between MOF-FA and MOF-FA-def1 while the CO_2 adsorption enthalpy of MOF-FA-def3 is slightly lower than that of MOF-FA but still significantly higher than the adsorption enthalpy of MOF-TFA, indicating that the sole effect of defects on the CO_2 adsorption is rather limited in MOF-FA.

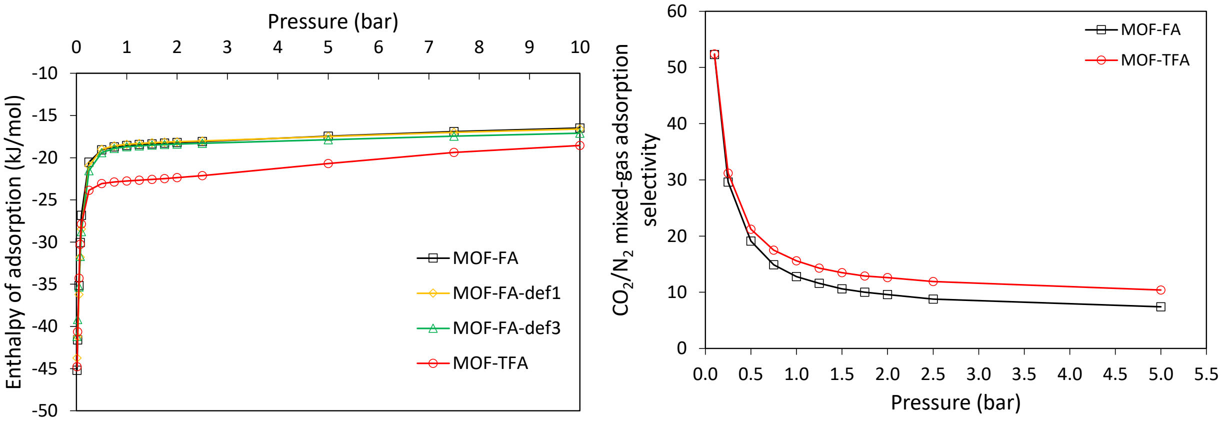

Figure 8: Simulated CO_2 adsorption enthalpies for MOF-FA, MOF-TFA and MOF-FA with 1 and 3 defects, respectively (left). Simulated mixed-gas adsorption CO_2/N_2 selectivities for MOF-FA and MOF-TFA (right).

3.3 Gas permeation

CO_2 permeability of the mixed-gas experiments with 15v%/85v% and 50v%/50v% CO_2/N_2 feed compositions and of the CO_2 pure gas experiment is given in Figure 9. All MMMs show a significantly higher CO_2 permeability for all feed compositions compared to the pristine Matrimid membrane, owing to the incorporation of the MOF[71,72]. For the 15v%/85v% CO_2/N_2, the 50v%/50v% CO_2/N_2 and the pure CO_2 data, respectively, the smallest permeability increase was observed for MMM-Li_2SO_4 (+23%, +20%, +15%) while the most substantial increase was recorded for MMMs containing MOF-TFA (+52%, +72%, +72%) as a result of a substantially increased CO_2 solubility upon incorporation of the TFA functionalized MOF (+33%). The low MMM-Li_2SO_4 permeability can be linked to the above-mentioned pore blockage by Li_2SO_4 deposition. Furthermore, a similar trend can be seen for the various feed conditions with the CO_2 permeability increasing in the order Matrimid < MMM-Li_2SO_4 < MMM-His ≈ MMM-GA ≈ MMM-BA ≈ MMM-FA < MMM-TFA. Finally, the CO_2 permeability is reduced when the CO_2 content in the feed is increased from 15% to 50% and eventually to 100%. A similar trend was observed for UiO-66-NH_2 MMMs based on various fluorinated polyimides[11,19,73]. These observations are in line with the dual-mode sorption model, which predicts saturation of polymer excess free volume elements at elevated CO_2 pressure, resulting in a lowered CO_2 solubility[74,75].

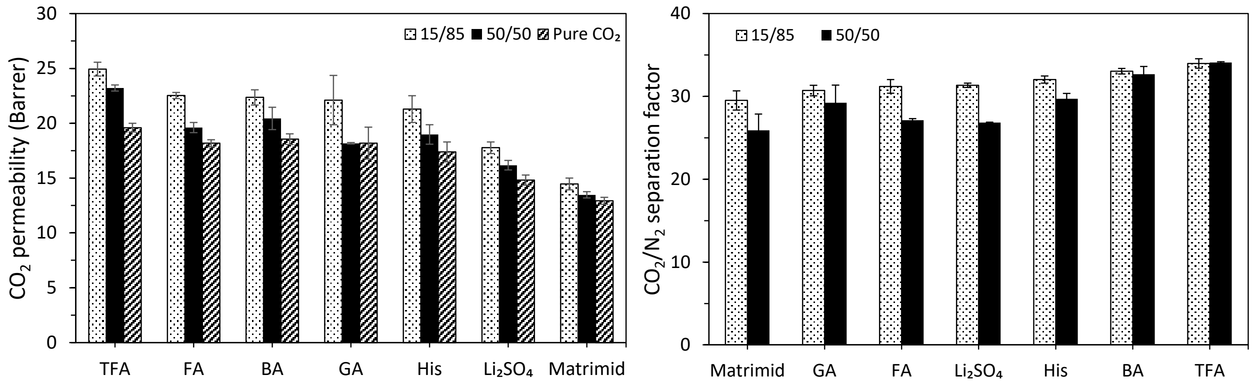

Figure 9: CO_2 permeability (left) and CO_2/N_2 separation factor (right) for the 15v%/85v% and 50v%/50v% mixed-gas CO_2/N_2 experiment and the CO_2 pure gas experiment of all membranes. Gas filtrations were performed at 30 °C and 5 bar feed pressure. All MMMs contain 10 wt.% MOF.

The CO_2/N_2 separation factors of Matrimid (Figure 9) for the 15v%/85v% (29.5) and the 50v%/50v% feed (25.9) are similar to literature[76,77]. In general, incorporation of the functionalized MOFs leads to a small enhancement in CO_2/N_2 separation factor for both feed mixtures compared to the pristine Matrimid membrane, but only small differences can be noticed between the MMMs. DSC measurements confirmed a similar increase in T_g for all MMMs. This indicates a certain (and similar) degree of polymer rigidification at the polymer/particle interface, thus (partially) explaining the elevated MMM separation factor. In addition, since no differences in particle morphology or particle size were observed with SEM (all MOFs were synthesized starting from the same MOF-FA batch), it is reasonable to assume that polymer rigidification is comparable for all MMMs. Similar to the permeability measurements, MOF-TFA causes the largest improvement of the separation factor of all MOFs, while MOF-GA, MOF-Li_2SO_4 and MOF-FA do not significantly affect the 15v%/85v% and 50v%/50v% separation factor. Functionalization with TFA (+9%, +25%) results in the best performance (compared to MMM-FA), which can be explained by the improved CO_2/N_2 selectivity for MOF-TFA (as was confirmed by the GCMC simulations) and the resulting increasing in solubility selectivity for MMM-TFA. As mentioned earlier, it is believed that the strongly polarized C-F bonds in MOF-TFA and the consequent higher CO_2 affinity are at the base of the good separation factor for MMM-TFA[10]. This was confirmed by both experimental and simulated CO_2 adsorption enthalpies, which were significantly lower (stronger MOF-CO_2 interaction) upon functionalization with TFA and eventually resulted in an enhanced CO_2/N_2 mixed-gas adsorption selectivity for MOF-TFA compared to MOF-FA (Figure 8). For the BA functionalized MOF, MMM-BA probably profits from enhanced π-π interaction between phenyl groups at the MOF surface and aromatic moieties of the polymer chains, which has previously been reported to improve polymer-MOF compatibility and, as a result, the separation factor[78]. It can be hypothesized that a higher CO_2 Q_{st} might lead to a higher selectivity for the MMM based on MOF-TFA, but observations for MOF-BA (with the lowest $Q_{st,0}$ but second highest α^*) contradict this. Finally, a lowered CO_2/N_2 selectivity for the 50v%/50v% feed is expected based on the dual-sorption model as the N_2 partial pressure is reduced (higher N_2 permeability), while the CO_2 partial pressure is enhanced (lower CO_2 permeability)[75].

3.4 Correlation of MOF parameters with membrane CO_2 permeation

Overall, the effect of ligand type on the MMM CO_2 permeability and CO_2/N_2 separation factor strongly varies when compared to the MOF-FA starting material. Only functionalization with TFA and Li_2SO_4 causes the MMM permeability to change significantly while improved separation factors with respect to MOF-FA are only observed for BA and TFA functionalization. To quantify the relationship between the examined MOF properties and the MMM permeation behavior, correlation coefficients between these parameters have been calculated in Table 2. Results were interpreted based on statistic guidelines defined by Ross *et al.*[79]. Correlation coefficients lower than 0.30 are considered as weak correlations, between 0.30 and 0.80 as moderate and higher than 0.80 as strong.

The conventional MOF parameters (BET surface area and pore volume) display a moderate linear correlation with the obtained permeabilities. This seems reasonable, owing to the positive relationship between gas diffusivity and MMM free volume[75]. In addition, a weak correlation is observed between these parameters and the CO_2/N_2 separation factor. Unexpectedly, also CO_2 uptake in both the low (at 50 mbar) and high (at 1000 mbar) pressure region correlates very poorly with both separation factors, while only moderate correlations were noted with permeability in 15v%/85v%, 50v%/50v% and pure CO_2 feed. This strongly contrasts with literature, where a high CO_2 uptake is very frequently used to explain MMM permeation observations[27,80]. The correlation of Q_{st} on one hand with CO_2 permeability and CO_2/N_2 separation factor on the other hand is less straightforward to interpret. The adsorption enthalpy at zero coverage ($Q_{st,0}$) shows moderate correlation with the CO_2 permeabilities, comparable to the CO_2 uptake values. Similarly, only weak correlations are observed for $Q_{st,0}$ and the different separation factors. Interestingly, strong correlations are observed between $Q_{st,15}$ and $Q_{st,30}$ on one hand and $P_{15/85}$, $P_{50/50}$ and $P_{100/0}$ on the other hand while correlation coefficients of $Q_{st,15}$ and $Q_{st,30}$ with the $\alpha^*_{15/85}$ and $\alpha^*_{50/50}$ are higher than for CO_2 uptake but are still considered only moderate. As such, Q_{st} can be considered as the most effective predictor for MMM CO_2 permeability amongst all MOF parameters.

A possible explanation for the difference in correlation strength of the Q_{st} at low loading and the ones at high loading might be found in the existence of mobile and immobile gas species in the membrane[81]. $Q_{st,0}$ represents the adsorption enthalpy of the high affinity sorption sites in the MOF and can possibly be linked to the tetragonal cages, which are the primary CO_2 sorption sites (marked as site 1 in Figure 6 and Figure 7) at very low CO_2 pressure. These sites correspond with highly negative CO_2 adsorption enthalpies (very strong MOF-CO_2 interaction) and the highest CO_2/N_2 mixed-gas adsorption selectivity values observed (up to 60, Figure 8). Moreover, they are present in both MOF-FA and MOF-TFA (and, by extension, in all functionalized MOF-808 samples), explaining the very similar enthalpy and selectivity values for both MOFs at low CO_2 pressures. At relatively higher CO_2 pressures (starting from 0.25 bar in Figure 8), the GCMC simulations show substantial differences in adsorption enthalpy and CO_2/N_2 adsorption selectivities between MOF-FA and MOF-TFA caused by the increased influence of the second type of adsorption sites (marked as site 2 in Figure 6 and Figure 7). It can thus be hypothesized that these sites (partially) immobilize gas molecules through (too) strong binding interaction[26] and thus do not (or to a lesser extent) contribute to gas permeation through the membrane. Although this hypothesis should be proven by performing time-lag experiments, it would explain the observed difference in correlation coefficients for $Q_{st,0}$ and $Q_{st,30}$[81].

As the overall gas permeability through the MMM is a net result of both MOF and polymer properties and their mutual interactions, it is not unexpected that none of the MOF parameters can predict the trends in MMM permeability one-on-one. Nonetheless, the unanticipated lack of correlation for CO_2 permeability with CO_2 uptake and its strong correlation with $Q_{st,15}$ and $Q_{st,30}$ once more underline the difficulty to formulate strong and general guidelines to steer MMM design and, more importantly, the need for more research aiming at finding consistent relationships between MOF and MMM structures and ultimate membrane performance.

Table 2: Correlation coefficients between MOF-808 parameters (CO_2 uptake at 50 and 1000 mbar and Q_{st} at a coverage of 0, 15, 30 cm^3 (STP)/g)) and the corresponding MMM parameters (α^* at 15v%/85v% and 50v%/50v% CO_2/N_2 feed, and CO_2 permeabilities for 15v%/85v% and 50v%/50v% CO_2/N_2 feed and the pure CO_2 feed ($P_{100/0}$)). Strong correlations are indicated in green and weak correlations in red. Intermediate correlations have no special markings.

	CO_2 uptake (50 mbar)	**CO_2 uptake (1000 mbar)**	**BET surface area**	**Pore volume**	**$Q_{st,0}$**	**$Q_{st,15}$**	**$Q_{st,30}$**
$\alpha^*_{15/85}$	0.079	0.053	0.123	0.173	0.056	0.414	0.291
$\alpha^*_{50/50}$	0.010	0.106	0.126	0.230	0.222	0.368	0.423
$P_{15/85}$	0.431	0.658	0.722	**0.800**	0.513	0.756	**0.834**
$P_{50/50}$	0.532	0.558	0.681	0.733	0.473	**0.844**	0.793
$P_{100/0}$	0.352	0.665	0.622	0.716	0.433	0.715	**0.866**

4 Conclusions

An attempt was made to fundamentally correlate MOF-808 parameters with the CO_2/N_2 separation performance indicators of the corresponding MMMs. More specifically, MOF CO_2 uptake, CO_2 Q_{st} at different CO_2 loading, pore volume and BET surface area were correlated with the MMM CO_2/N_2 separation factor and CO_2 permeability under varying feed conditions. Post-synthetic functionalization of FA modulated MOF-808 with different ligands (i.e. TFA, BA, GA, histidine and Li_2SO_4) proved to be a successful tool to influence this set of MOF parameters, leading to a broad range of systematically varying parameter values for BET surface area, pore volume, CO_2 uptake and CO_2 Q_{st}. For the different MOF-808 MMMs tested in this work, MOF CO_2 uptake was a poor predictor for MMM performance, showing a very weak correlation with CO_2/N_2 separation factor and only moderate correlation with CO_2 permeability. This is in contrast to literature where CO_2 uptake is one of the dominant factors used to explain MMM separation behavior. The loading-dependent CO_2 Q_{st} correlates substantially better with the membrane performance indicators than the CO_2 uptake. Correlation coefficients of $Q_{st,15}$ and $Q_{st,30}$ with the separation factor were higher than for CO_2 uptake, but were still considered only moderate. A strong correlation was however found between $Q_{st,15}$ and $Q_{st,30}$ on one hand and $P_{15/85}$, $P_{50/50}$ and $P_{0/100}$ on the other hand, indicating that Q_{st} can be considered as the most effective predictor for MMM CO_2 permeability amongst the MOF parameters. Interestingly, Q_{st} at zero coverage failed to show a strong correlation with the MMM performance indicators. GCMC simulations on MOF-FA and MOF-TFA revealed the existence of 2 types of adsorption sites in MOF-808. The first type of adsorption type is independent of cluster functionalization (e.g. TFA instead of FA) and corresponds with the tetragonal 'linker' cage, resulting in very strong MOF-CO_2 interaction (highly negative adsorption enthalpies) even at low CO_2 pressures while the second type of adsorption site was shown to be susceptible to TFA functionalization. Finally, the existence of different adsorption sites with varying adsorption enthalpies was linked to the observed difference in correlation coefficients for $Q_{st,0}$ and $Q_{st,30}$ with CO_2 permeability.

Author information

Corresponding author: prof. Ivo Vankelecom

E-mail: ivo.vankelecom@kuleuven.be

Tel: +32 16 32 15 94

Conflicts of interest

There are no conflicts to declare.

Acknowledgments

R.T., N.V.V. and A.L. acknowledge the FWO for their support through a(n) (SB-)PhD fellowship (1S63317N, 1S32917N and 11D2220N). A.L. and V.V.S. would also like to thank the Research Board of Ghent University (BOF) for their support and the European Union's Horizon 2020 Research and Innovation Programme [ERC Consolidator Grant Agreement 647755 – DYNPOR (2015-2020)] for the received funding. The computational resources (Stevin Supercomputer Infrastructure) and services used in this work were provided by the VSC (Flemish Supercomputer Center), funded by Ghent University, FWO and the Flemish Government – department EWI.

References

(1) Seoane, B.; Coronas, J.; Gascon, I.; Benavides, M. E.; Karvan, O.; Caro, J.; Kapteijn, F.; Gascon, J. Metal–Organic Framework Based Mixed Matrix Membranes: A Solution for Highly Efficient CO2 Capture? Chem. Soc. Rev. 2015, 44, 2421–2454. https://doi.org/10.1039/C4CS00437J.

(2) Rezakazemi, M.; Ebadi Amooghin, A.; Montazer-Rahmati, M. M.; Ismail, A. F.; Matsuura, T. State-of-the-Art Membrane Based CO2separation Using Mixed Matrix Membranes (MMMs): An Overview on Current Status and Future Directions. Prog. Polym. Sci. 2014, 39 (5), 817–861. https://doi.org/10.1016/j.progpolymsci.2014.01.003.

(3) Vanherck, K.; Koeckelberghs, G.; Vankelecom, I. F. J. Crosslinking Polyimides for Membrane Applications: A Review. Prog. Polym. Sci. 2013, 38 (6), 874–896. https://doi.org/10.1016/j.progpolymsci.2012.11.001.

(4) Liang, C. Z.; Chung, T.-S.; Lai, J.-Y. A Review of Polymeric Composite Membranes for Gas Separation and Energy Production. Prog. Polym. Sci. 2019, 97, 101141. https://doi.org/10.1016/j.progpolymsci.2019.06.001.

(5) Li, H.; Haas-Santo, K.; Schygulla, U.; Dittmeyer, R. Inorganic Microporous Membranes for H2 and CO2 Separation — Review of Experimental and Modeling Progress. Chem. Eng. Sci. 2015, 127, 401–417. https://doi.org/10.1016/j.ces.2015.01.022.

(6) Tsapatsis, M. Toward High-Throughput Zeolite Membranes. Science (80-.). 2011, 334 (November), 767–769. https://doi.org/10.1126/science.1205957.

(7) Qian, Q.; Chi, W. S.; Han, G.; Smith, Z. P. Impact of Post-Synthetic Modification Routes on Filler Structure and Performance in Metal–Organic Framework-Based Mixed-Matrix Membranes. Indust 2020, 59, 5432–5438. https://doi.org/10.1021/acs.iecr.9b04820.

(8) Chi, W. S.; Sundell, B. J.; Zhang, K.; Harrigan, D. J.; Hayden, S. C.; Smith, Z. P. Mixed-Matrix Membranes Formed from Multi-Dimensional Metal–Organic Frameworks for Enhanced Gas Transport and Plasticization Resistance. ChemSusChem 2019, 02139, 2355–2360. https://doi.org/10.1002/cssc.201900623.

(9) Shahid, S.; Nijmeijer, K. Performance and Plasticization Behavior of Polymer-MOF Membranes for Gas Separation at Elevated Pressures. J. Memb. Sci. 2014, 470, 166–177. https://doi.org/10.1016/j.memsci.2014.07.034.

(10) Thür, R.; Van Velthoven, N.; Lemmens, V.; Bastin, M.; Smolders, S.; De Vos, D. De; Vankelecom, I. F. J. Modulator-Mediated Functionalization of MOF-808 as a Platform Tool to Create High-Performance Mixed-Matrix Membranes. ACS Appl. Mater. Interfaces 2019. https://doi.org/10.1021/acsami.9b19774.

(11) Ahmad, M. Z.; Peters, T. A.; Konnertz, N. M.; Visser, T.; Téllez, C.; Coronas, J.; Fila, V.; de Vos, W. M.; Benes, N. E. High-Pressure CO2/CH4 Separation of Zr-MOFs Based Mixed Matrix Membranes. Sep. Purif. Technol. 2020, 230 (June 2019), 115858. https://doi.org/10.1016/j.seppur.2019.115858.

(12) Dong, G.; Li, H.; Chen, V. Challenges and Opportunities for Mixed-Matrix Membranes for Gas Separation. J. Mater. Chem. A 2013, 1 (15), 4610–4630. https://doi.org/10.1039/C3TA00927K.

(13) Van Essen, M.; Montrée, E.; Houben, M.; Borneman, Z.; Nijmeijer, K. Magnetically Aligned and Enriched Pathways of Zeolitic Imidazolate Framework 8 in Matrimid Mixed Matrix Membranes for Enhanced CO 2 Permeability. Membranes (Basel). 2020, 10 (7), 155.

(14) Rodenas, T.; Van Dalen, M.; García-Pérez, E.; Serra-Crespo, P.; Zornoza, B.; Kapteijn, F.; Gascon, J. Visualizing MOF Mixed Matrix Membranes at the Nanoscale: Towards Structure-Performance Relationships in CO2/CH4 Separation Over NH2-MIL-53 (Al)@PI. Adv. Funct. Mater. 2014, 24, 249–256. https://doi.org/10.1002/adfm.201203462.

(15) Ozcan, A.; Semino, R.; Maurin, G.; Yazaydin, A. O. Modeling of Gas Transport through Polymer/MOF Interfaces: A Microsecond-Scale Concentration Gradient-Driven Molecular Dynamics Study. Chem. Mater. 2020, 32, 1288–1296. https://doi.org/10.1021/acs.chemmater.9b04907.

(16) Kang, Z.; Peng, Y.; Hu, Z.; Qian, Y.; Chi, C.; Yeo, L. Y.; Tee, L.; Zhao, D. Mixed Matrix Membranes Composed of Two-Dimensional Metal–Organic Framework Nanosheets for Pre-Combustion CO2 Capture: A Relationship Study of Fi Ller Morphology versus Membrane. J. Mater. Chem. A 2015, 3, 20801–20810. https://doi.org/10.1039/c5ta03739e.

(17) Chen, K.; Xu, K.; Xiang, L.; Dong, X.; Han, Y.; Wang, C.; Sun, L.; Pan, Y. Enhanced CO2/CH4 Separation Performance of Mixed-Matrix Membranes through Dispersion of Sorption-Selective MOF Nanocrystals. J. Memb. Sci. 2018, 563 (March), 360–370. https://doi.org/10.1016/j.memsci.2018.06.007.

(18) Cheng, Y.; Ying, Y.; Zhai, L.; Liu, G.; Dong, J.; Wang, Y.; Christopher, M. P.; Long, S.; Wang, Y.; Zhao, D. Mixed Matrix Membranes Containing MOF@COF Hybrid Fillers for Efficient CO2/CH4 Separation. J. Memb. Sci. 2019, 573 (November 2018), 97–106. https://doi.org/10.1016/j.memsci.2018.11.060.

(19) Qian, Q.; Wu, A. X.; Chi, W. S.; Asinger, P. A.; Lin, S.; Hypsher, A.; Smith, Z. P. Mixed-Matrix Membranes Formed from Imide-Functionalized UiO-66-NH2 for Improved Interfacial Compatibility. ACS Appl. Mater. Interfaces 2019, 11, 31257–31269. https://doi.org/10.1021/acsami.9b07500.

(20) Thür, R.; Van Velthoven, N.; Slootmaekers, S.; Didden, J.; Verbeke, R.; Smolders, S.; Egger, W.; Dickmann, M.; De Vos, D.; Vankelecom, I. F. J. Bipyridine-Based UiO-67 as Novel Filler in Mixed-Matrix Membranes for CO2-Selective Gas Separation. J. Memb. Sci. 2019, 576 (15 April 2019), 78–87. https://doi.org/10.1016/j.memsci.2019.01.016.

(21) Yu, G.; Li, Y.; Wang, Z.; Xiaoteng, T.; Zhu, G.; Zou, X. Mixed Matrix Membranes Derived from Nanoscale Porous Organic Frameworks for Permeable and Selective CO2 Separation. J. Memb. Sci. 2019, 591 (August), 117343. https://doi.org/10.1016/j.memsci.2019.117343.

(22) Jia, C.; Cirujano, F. G.; Bueken, B.; Claes, B.; Jonckheere, D.; Van Geem, K. M.; De Vos, D. Geminal Coordinatively Unsaturated Sites on MOF-808 for the Selective Uptake of Phenolics from a Real Bio-Oil Mixture. ChemSusChem 2019, 101, 1256–1266. https://doi.org/10.1002/cssc.201802692.

(23) Van Velthoven, N.; Henrion, M.; Dallenes, J.; Krajnc, A.; Bugaev, A. L.; Liu, P.; Bals, S.; Soldatov, A. V; Vos, D. E. De. S,O-Functionalized Metal−Organic Frameworks as Heterogeneous Single-Site Catalysts for the Oxidative Alkenylation of Arenes via C−H Activation. ACS Catal. 2020, 10, 5077–5085. https://doi.org/10.1021/acscatal.0c00801.

(24) Reinsch, H.; Waitschat, S.; Chavan, S. M.; Lillerud, K. P.; Stock, N. A Facile "Green" Route for Scalable Batch Production and Continuous Synthesis of Zirconium MOFs. Eur. J. Inorg. Chem. 2016, 2016 (27), 4490–4498. https://doi.org/10.1002/ejic.201600295.

(25) Sanders, D. F.; Smith, Z. P.; Guo, R.; Robeson, L. M.; McGrath, J. E.; Paul, D. R.; Freeman, B. D. Energy-Efficient Polymeric Gas Separation Membranes for a Sustainable Future: A Review. Polymer (Guildf). 2013, 54 (18), 4729–4761. https://doi.org/10.1016/j.polymer.2013.05.075.

(26) Galizia, M.; Chi, W. S.; Smith, Z. P.; Merkel, T. C.; Baker, R. W.; Freeman, B. D. Polymers and Mixed Matrix Membranes for Gas and Vapor Separation : A Review and Prospective Opportunities. Macromolecules 2017, 50, 7809–7843. https://doi.org/10.1021/acs.macromol.7b01718.

(27) Qian, Q.; Asinger, P. A.; Lee, M. J.; Han, G.; Rodriguez, K. M.; Lin, S.; Benedetti, F. M.; Wu, A. X.; Chi, W. S.; Smith, Z. P. MOF-Based Membranes for Gas Separations. Chem. Rev. 2020, 120 (16), 8161. https://doi.org/10.1021/acs.chemrev.0c00119.

(28) Baek, J.; Rungtaweevoranit, B.; Pei, X.; Park, M.; Fakra, S. C.; Liu, Y.-S.; Matheu, R.; Alshmimri, S. A.; Alshehri, S.; Trickett, C. A.; et al. Bioinspired Metal–Organic Framework Catalysts for Selective Methane Oxidation to Methanol. J. Am. Chem. Soc. 2018, 140, 18208–18216. https://doi.org/10.1021/jacs.8b11525.

(29) Rouquerol, F.; Rouquerol, J.; Sing, K. Adsorption by Powders and Porous Solids, 11th ed.; Academic Press: San Diego, 1999.

(30) Walton, K. S.; Snurr, R. Q. Applicability of the BET Method for Determining Surface Areas of Microporous Metal-Organic Frameworks. J. Am. Chem. Soc. 2007, 129 (27), 8552–8556. https://doi.org/10.1021/ja071174k.

(31) Park, H. J.; Suh, M. P. Enhanced Isosteric Heat, Selectivity and Uptake Capacity of CO2 Adsorption in a Metal-Organic Framework by Impregnated Metal Ions. Chem. Sci. 2013, 4 (3), 685–690. https://doi.org/10.1039/c2sc21253f.

(32) Hutter, J.; Iannuzzi, M.; Schiffmann, F.; VandeVondele, J. Cp2k: Atomistic Simulations of Condensed Matter Systems. WIREs Comput. Mol. Sci. 2013, 4 (1), 15–25.

(33) Perdew, J. P.; Burke, K.; Ernzerhof, M. Generalized Gradient Approximation Made Simple. Phys. Rev. Lett. 1996, 77 (3), 3865–3868.

(34) Grimme, S.; Antony, J.; Ehrlich, S.; Krieg, H. A Consistent and Accurate Ab Initio Parametrization of Density Functional Dispersion Correction (DFT-D) for the 94 Elements H-Pu. J. Phys. Chem. 2010, 132, 154104.

(35) Grimme, S.; Ehrlich, S.; Goerigk, L. Effect of the Damping Function in Dispersion Corrected Density Functional Theory. J. Comput. Chem. 2011, 32 (7), 1456–1465.

(36) VandeVondele, J.; Hutter, J. Gaussian Basis Sets for Accurate Calculations on Molecular Systems in Gas and Condensed Phases. J. Chem. Phys. 2007, 127 (11), 114105.

(37) Goedecker, S.; Teter, M.; Hutter, J. Separable Dual-Space Gaussian Pseudopotentials. Phys. Rev. B 1996, 54, 1703–1710.

(38) Dubbeldam, D.; Calero, S.; Ellis, D. E.; Snurr, R. Q. RASPA: Molecular Simulation Software for Adsorption and Diffusion in Flexible Nanoporous Materials. Mol. Simulations 2016, 42 (2), 81–101.

(39) Potoff, J. J.; Siepmann, J. I. Vapor-Liquid Equilibria of Mixtures Containing Alkanes, Carbon Dioxide, and Nitrogen. AlChE J. 2004, 47 (7), 1676–1682.

(40) Verstraelen, T.; Vandenbrande, S.; Heidar-Zadeh, F.; Vanduyfhuys, L.; Van Speybroeck, V.; Waroquier, M.; Ayers, P. W. Minimal Basis Iterative Stockholder: Atoms in Molecules for Force- Field Development. J. Chem. Theory Comput. 2016, 12, 3894–3912. https://doi.org/10.1021/acs.jctc.6b00456.

(41) Mayo, S. L.; Olafson, B. D.; Goddard, W. A. DREIDING: A Generic Force Field for Molecular Simulations. J. Phys. Chem. 1990, 94 (26), 8897–8909.

(42) Vandenbrande, S.; Verstraelen, T.; Gutiérrez-Sevillano, J. J.; Waroquier, M.; Van Speybroeck, V. Van. Methane Adsorption in Zr-Based MOFs: Comparison and Critical Evaluation of Force Fields. J. Phys. Chem. C 2017, 121 (45), 25309–25322. https://doi.org/10.1021/acs.jpcc.7b08971.

(43) Rappe, A. K.; Casewit, C. J.; Colwell, K. S.; Goddard III, W. A.; Skiff, W. M. UFF, a Full Periodic Table Force Field for Molecular Mechanics and Molecular Dynamics Simulations. J. Am. Chem. Soc. 1992, 114 (25), 10024–10035.

(44) Khan, A. L.; Basu, S.; Cano-odena, A.; Vankelecom, I. F. J. Novel High Throughput Equipment for Membrane-Based Gas Separations. J. Memb. Sci. 2010, 354 (1–2), 32–39. https://doi.org/10.1016/j.memsci.2010.02.069.

(45) Didden, J.; Thür, R.; Volodin, A.; Vankelecom, I. F. J. Blending PPO-Based Molecules with Pebax MH 1657 in Membranes for Gas Separation. J. Appl. Polym. Sci. 2018, 135, 46433. https://doi.org/10.1002/app.46433.

(46) Thür, R.; Lemmens, V.; Van Havere, D.; van Essen, M.; Nijmeijer, K.; Vankelecom, I. F. J. Tuning 6FDA-DABA Membrane Performance for CO2 Removal by Physical Densification and Decarboxylation Cross-Linking during Simple Thermal Treatment. J. Memb. Sci. 2020, 610, 118195. https://doi.org/10.1016/j.memsci.2020.118195.

(47) Hafizovic, J.; Bjørgen, M.; Olsbye, U.; Dietzel, P. D. C.; Bordiga, S.; Prestipino, C.; Lamberti, C.; Lillerud, K. P. The Inconsistency in Adsorption Properties and Powder XRD Data of MOF-5 Is Rationalized

by Framework Interpenetration and the Presence of Organic and Inorganic Species in the Nanocavities. J. Am. Chem. Soc. 2007, No. 7, 3612–3620. https://doi.org/10.1021/ja0675447.

(48) Øien-ØDegaard, S.; Shearer, G. C.; Wragg, D. S.; Lillerud, K. P. Pitfalls in Metal–Organic Framework Crystallography: Towards More Accurate. Chem. Soc. Rev. 2017, 46, 4867–4876. https://doi.org/10.1039/c6cs00533k.

(49) Chen, B.; Wang, X.; Zhang, Q.; Xi, X.; Cai, J.; Qi, H.; Shi, S.; Wang, J.; Yuan, D.; Fang, M. Synthesis and Characterization of the Interpenetrated MOF-5 †. J. Mater. Chem. 2010, 20, 3758–3767. https://doi.org/10.1039/b922528e.

(50) Xuan, K.; Pu, Y.; Li, F.; Luo, J.; Zhao, N.; Xiao, F. Metal-Organic Frameworks MOF-808-X as Highly Efficient Catalysts for Direct Synthesis of Dimethyl Carbonate from CO2 and Methanol. Chinese J. Catal. 2019, 40, 533–566. https://doi.org/doi:10.1016/S1872-2067(19)63291-2.

(51) Jiang, Y.; Liu, C.; Caro, J.; Huang, A. A New UiO-66-NH2 Based Mixed-Matrix Membranes with High CO2/CH4 Separation Performance. Microporous Mesoporous Mater. 2019, 274 (July 2018), 203–211. https://doi.org/10.1016/j.micromeso.2018.08.003.

(52) Smith, B. C. Infrared Spectral Interpretation: A Systematic Approach; CRC Press LLC, 1998.

(53) Kumar, S.; Rai, A. K.; Rai, S. B.; Rai, D. K. Infrared and Raman Spectra of Histidine: An Ab Initio DFT Calculations of Histidine Molecule and Its Different Protonated Forms. Indian J. Phys. 2010, 84, 563–573. https://doi.org/doi:10.1007/s12648-010-0039-6.

(54) Stepanian, S. G.; Reva, I. D.; Radchenko, E. D.; Sheina, G. G. Infrared Spectra of Benzoic Acid Monomers and Dimers in Argon Matrix. Vib. Spectrosc. 1996, 11, 123–133. https://doi.org/doi:10.1016/0924-2031(95)00068-2.

(55) Jiang, J.; Gándara, F.; Zhang, Y.-B.; Na, K.; Yaghi, O. M.; Klemperer, W. G. Superacidity in Sulfated Metal − Organic Framework-808. J. Am. Chem. Soc. 2014, 136, 12844–12847. https://doi.org/10.1021/ja507119n.

(56) Williams, R.; Jencks, W. P.; Westheimer, F. H. PKa Data Compiled by R. Williams.

(57) Fan, G.; Liu, Y.; Wang, H. Identification of Thermophilic Proteins by Incorporating Evolutionary and Acid Dissociation Information into Chou's General Pseudo Amino Acid Composition. J. Theor. Biol. 2016, 407, 138–142. https://doi.org/10.1016/j.jtbi.2016.07.010.

(58) Xu, J.; Liu, J.; Wang, X.; Xu, Y.; Chen, S.; Wang, X. Optimized Synthesis of Zr(IV) Metal Organic Frameworks (MOFs-808) for Efficient Hydrogen Storage. New J. Chem. 2019, 43 (2), 4092–4099. https://doi.org/10.1039/c8nj06362a.

(59) Wendy, S.; Queen, L. An Experimental and Computational Study of CO2 Adsorption in the Sodalite-Type M-BTT (M ¼ Cr, Mn, Fe, Cu) Metal–Organic Frameworks Featuring Open Metal Sites. Chem. Sci. 2018, 9, 4579. https://doi.org/10.1039/c8sc00971f.

(60) Xue, D.-X.; Cairns, A. J.; Belmabkhout, Y.; Wojtas, L.; Liu, Y.; Alkordi, M. H.; Eddaoudi, M. Tunable Rare-Earth Fcu-MOFs: A Platform for Systematic Enhancement of CO2 Adsorption Energetics and Uptake. J. Am. Chem. Soc. 2013, 135, 7660–7667. https://doi.org/10.1021/ja401429x.

(61) Cho, H.-Y.; Yang, D.-A.; Kim, J.; Jeong, S.-Y.; Ahn, W.-S. CO2 Adsorption and Catalytic Application of Co-MOF-74 Synthesized by Microwave Heating. Catal. Today 2012, 185 (1), 35–40. https://doi.org/10.1016/j.cattod.2011.08.019.

(62) Arstad, B.; Fjellvåg, H.; Kongshaug, K. O.; Swang, O.; Blom, R. Amine Functionalised Metal Organic Frameworks (MOFs) as Adsorbents for Carbon Dioxide. Adsorption 2008, 14, 755–762. https://doi.org/10.1007/s10450-008-9137-6.

(63) Mason, J. A.; Sumida, K.; Herm, Z. R.; Krishna, R.; Long, J. R. Evaluating Metal – Organic Frameworks for Post-Combustion Carbon Dioxide Capture via Temperature Swing Adsorption †. Energy Environ. Sci. 2011, 4, 3030–3040. https://doi.org/10.1039/c1ee01720a.

(64) Hossain, M. I.; Cunningham, J. D.; Becker, T. M.; Grabicka, B. E.; Walton, K. S.; Rabideau, B. D.; Glover, T. G. Impact of MOF Defects on the Binary Adsorption of CO2 and Water in UiO-66. Chem. Eng. Sci. 2019, 203, 146–357. https://doi.org/doi:10.1016/j.ces.2019.03.053.

(65) Koutsianos, A.; Kazimierska, E.; Barron, A. R.; Taddei, M.; Andreoli, E. A New Approach to Enhancing the CO2 Capture Performance of Defective UiO-66 via Post-Synthetic Defect Exchange. Dalt. Trans. 2019, 48, 3349–3359. https://doi.org/10.1039/c9dt00154a.

(66) Deria, P.; Mondloch, J. E.; Tylianakis, E.; Ghosh, P.; Bury, W.; Snurr, R. Q.; Hupp, J. T.; Farha, O. K. Perfluoroalkane Functionalization of NU-1000 via Solvent-Assisted Ligand Incorporation: Synthesis and CO2 Adsorption Studies. J. Am. Chem. Soc. 2013, 14, 16801–16804. https://doi.org/10.1021/ja408959g.

(67) Plonka, A. M.; Grissom, T. G.; Musaev, D. G.; Balboa, A.; Gordon, W. O.; Collins-Wildman, D. L.; Ghose, S. K.; Tian, Y.; Ebrahim, A. M.; Mitchell, M. B.; et al. Effect of Carbon Dioxide on the Degradation of Chemical Warfare Agent Simulant in the Presence of Zr Metal Organic Framework MOF-808. Chem. Mater. 2019, 31, 9904–9914. https://doi.org/10.1021/acs.chemmater.9b04565.

(68) Luconi, L.; Mercuri, G.; Islamoglu, T.; Fermi, A.; Bergamini, G.; Giambastiani, G.; Rossin, A. Benzothiazolium-Functionalized NU-1000: A Versatile Material for Carbon Dioxide Adsorption and Cyanide Luminescence Sensing. J. Mater. Chem. C 2020. https://doi.org/10.1039/d0tc01436b.

(69) Grissom, T. G.; Driscoll, D. M.; Troya, D.; Sapienza, N. S.; Usov, P. M.; Morris, A. J.; Morris, J. R. Molecular-Level Insight into CO2 Adsorption on the Zirconium-Based Metal−Organic Framework, UiO-66: A Combined Spectroscopic and Computational Approach. J. Phys. Chem. C 2019, 123, 13731–13738. https://doi.org/10.1021/acs.jpcc.9b02513.

(70) Lau, C. H.; Babarao, R.; Hill, M. R. A Route to Drastic Increase of CO2 Uptake in Zr Metal Organic Framework UiO-66. Chem. Commun. 2013, 49 (207890), 3634–3637. https://doi.org/10.1039/c3cc40470f.

(71) Chung, T. S.; Jiang, L. Y.; Li, Y.; Kulprathipanja, S. Mixed Matrix Membranes (MMMs) Comprising Organic Polymers with Dispersed Inorganic Fillers for Gas Separation. Prog. Polym. Sci. 2007, 32 (4), 483–507. https://doi.org/10.1016/j.progpolymsci.2007.01.008.

(72) Ahn, J.; Chung, W. J.; Pinnau, I.; Song, J.; Du, N.; Robertson, G. P.; Guiver, M. D. Gas Transport Behavior of Mixed-Matrix Membranes Composed of Silica Nanoparticles in a Polymer of Intrinsic

Microporosity (PIM-1). J. Memb. Sci. 2010, 346 (2), 280–287. https://doi.org/10.1016/j.memsci.2009.09.047.

(73) Ma, C.; Urban, J. J. Enhanced CO2 Capture and Hydrogen Purification by Hydroxy Metal–Organic Framework/Polyimide Mixed Matrix Membranes. ChemSusChem 2019, 12, 1–8. https://doi.org/10.1002/cssc.201902248.

(74) Wijmans, J. G. H.; Baker, R. W. The Solution-Diffusion Model: A Unified Approach to Membrane Permeation; 2006. https://doi.org/10.1002/047002903X.ch5.

(75) Matteucci, S.; Yampolskii, Y.; Freeman, B. D.; Pinnau, I. Transport of Gases and Vapors in Glassy and Rubbery Polymers. In Materials Science of Membranes for Gas and Vapor Separation; 2006; pp 1–48.

(76) Dingel, T.; Tessema, M.; Venna, S. R.; Dahe, G.; Hopkinson, D. P.; El-kaderi, H. M.; Sekizkardes, A. K. Incorporation of Benzimidazole Linked Polymers into Matrimid to Yield Mixed Matrix Membranes with Enhanced CO2/N2 Selectivity. J. Memb. Sci. 2018, 554 (January), 90–96. https://doi.org/10.1016/j.memsci.2018.02.054.

(77) Shan, M.; Seoane, B.; Pustovarenko, A.; Wang, X.; Liu, X. Benzimidazole Linked Polymers (BILPs) in Mixed-Matrix Membranes: Influence of Filler Porosity on the CO2/N2 Separation Performance. J. Memb. Sci. 2018, 566 (May), 213–222. https://doi.org/10.1016/j.memsci.2018.08.023.

(78) Venna, S. R.; Lartey, M.; Li, T.; Spore, A.; Kumar, S.; Nulwala, H. B.; Luebke, D. R.; Rosi, L.; Albenze, E. Fabrication of MMMs with Improved Gas Separation Properties Using Externally-Functionalized MOF Particles. J. Mater. Chem. A 2015, 3, 5014–5022. https://doi.org/10.1039/C4TA05225K.

(79) Ross, S. Introduction to Probability and Statistics for Engineers and Scientists, 4th editio.; 2009.

(80) Vinoba, M.; Bhagiyalakshmi, M.; Alqaheem, Y.; Alomair, A. A.; Pérez, A.; Rana, M. S. Recent Progress of Fillers in Mixed Matrix Membranes for CO2 Separation: A Review. Sep. Purif. Technol. 2017, 188, 431–450. https://doi.org/10.1016/j.seppur.2017.07.051.

(81) Paul, D. R.; Koros, W. J. Effect of Partially Immobilizing Sorption on Permeability and the Diffusion Time Lag. J. Polym. Sci. 1976, 14, 675–685.

(82) Frisch, M. J.; Trucks, G. W.; Schlegel, H. B.; Scuseria, G. E.; Robb, M. A.; Cheeseman, J. R.; Scalmani, G.; Barone, V.; Petersson, G. A.; Nakatsuji, H.; et al. Gaussian 16 Revision C.01; Inc., G., Ed.; Wallingford CT, 2016.

(83) Becke, A. D. Density-functional Thermochemistry. III. The Role of Exact Exchange. J. Chem. Phys. 1993, 98, 5648.

(84) Krishnan, R.; Binkley, J. S.; Seeger, R.; Pople, J. A. Self-consistent Molecular Orbital Methods. XX. A Basis Set for Correlated Wave Functions. J. Chem. Phys. 1980, 72, 650.

(85) Hay, P. J.; Wadt, W. R. Ab Initio Effective Core Potentials for Molecular Calculations. Potentials for the Transition Metal Atoms Sc to Hg. J. Chem. Phys. 1985, 82, 270.

(86) Enkovaara, J.; Rostgaard, C.; Mortensen, J. J.; Chen, J.; Dulak, M.; Ferrighi, L.; Gavnholt, J.; Glinsvad, C.; Haikola, V.; Lehtovaara, L.; et al. Electronic Structure Calculations with GPAW: A Real-Space

Implementation of the Projector Augmented-Wave Method. Joural Phys. Condens. Matter 2010, 22, 253202. https://doi.org/10.1088/0953-8984/22/25/253202.

(87) Chen, J.; Martınez, T. J. QTPIE : Charge Transfer with Polarization Current Equalization. A Fluctuating Charge Model with Correct Asymptotics. Chem. Phys. Lett. 2007, 438, 315–320. https://doi.org/10.1016/j.cplett.2007.02.065.

(88) Mukherjee, S.; Manna, B.; Desai, A. V.; Yin, Y.; Krishna, R.; Babarao, R.; Ghosh, S. K.; Kitagawa, S.; Kitaura, R.; Noro, S. -i.; et al. Harnessing Lewis Acidic Open Metal Sites of Metal–Organic Frameworks: The Foremost Route to Achieve Highly Selective Benzene Sorption over Cyclohexane. Chem. Commun. 2016, 52 (53), 8215–8218. https://doi.org/10.1039/C6CC03015G.

(89) Van Essen, M.; Van Den Akker, L.; Thür, R.; Houben, M.; Vankelecom, I. F. J.; Borneman, Z.; Nijmeijer, K. The Influence of Pore Aperture , Volume and Functionality of Isoreticular Gmelinite Zeolitic Imidazolate Frameworks on the Mixed Gas CO2/N2 and CO2/CH4 Separation Performance in Mixed Matrix Membranes. Sep. Purif. Technol. 2021, 260 (November 2020), 118103. https://doi.org/10.1016/j.seppur.2020.118103.

(90) Essen, M. Van; Akker, L. Van Den; Thür, R.; Houben, M.; Vankelecom, I. F. J.; Borneman, Z.; Nijmeijer, K. Investigation of ZIF-78 Morphology and Feed Composition on the Mixed Gas CO2/N2 Separation Performance in Mixed Matrix Membranes. Adv. Mater. Interfaces 2020, 2001478. https://doi.org/10.1002/admi.202001478.

(91) Monteiro, B.; Nabais, A. R.; Casimiro, M. H.; Martins, A. P. S.; Francisco, R. O.; Neves, A.; Pereira, C. L. Impact on CO2/N2 and CO2/CH4 Separation Performance Using Cu-BTC with Supported Ionic Liquids-Based Mixed Matrix Membranes. Membranes (Basel). 2018, 8 (93), 11. https://doi.org/10.3390/membranes8040093.

(92) Marti, A. M.; Venna, S. R.; Roth, E. A.; Culp, T.; Hopkinson, D. P. Simple Fabrication Method for Mixed Matrix Membranes with in Situ MOF Growth for Gas Separation. ACS Appl. Mater. Interfaces 2018, 10, 24784–24790. https://doi.org/10.1021/acsami.8b06592.

5 Supporting information

Correlation of MOF-808 parameters to mixed-matrix membrane CO_2 permeation behavior

Raymond Thür[a], Daan Van Havere[a], Niels Van Velthoven[a], Simon Smolders[a], Aran Lamaire[b], Jelle Wieme[b], Veronique Van Speybroeck[b], Dirk De Vos[a], Ivo F.J. Vankelecom[a]

[a]Centre for Membrane Separations, Adsorption, Catalysis and Spectroscopy for Sustainable Solutions (cMACS), KU Leuven, Celestijnenlaan 200F, Box 2454, 3001 Heverlee, Belgium

[b]Center for Molecular Modeling, Ghent University, Tech Lane Ghent Science Park, Campus A, Technologiepark 46, 9052 Zwijnaarde, Belgium

E-mail: ivo.vankelecom@kuleuven.be

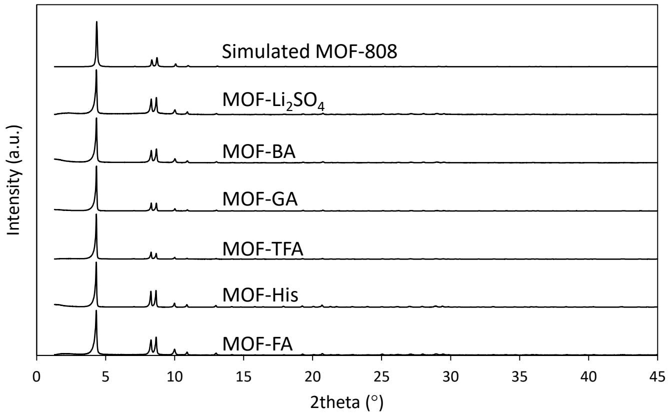

Figure S1~~1~~: XRD patterns of all MOF samples.

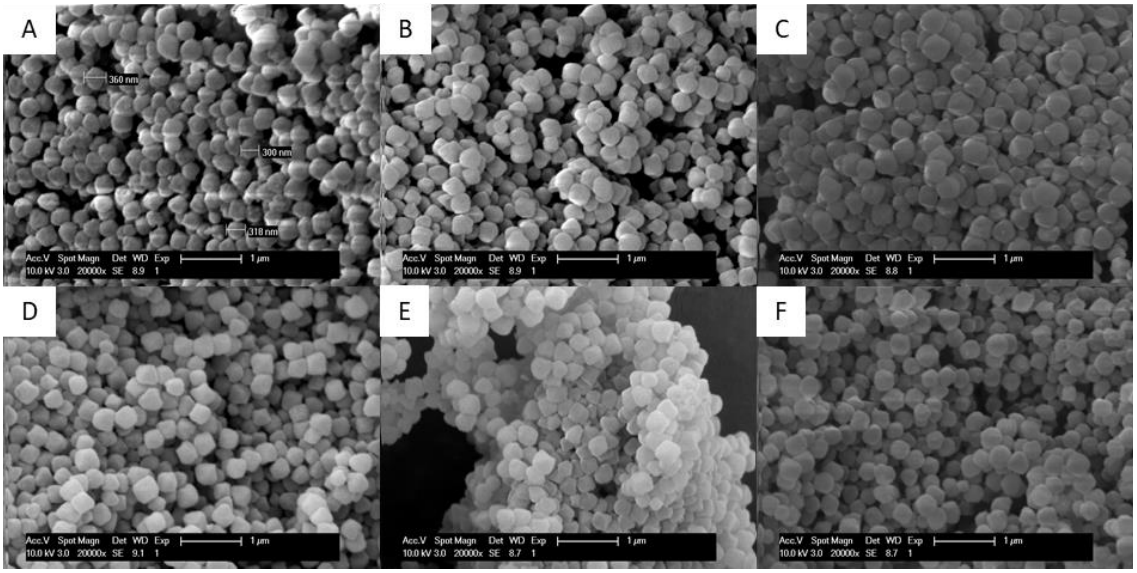

Figure S2~~2~~: SEM images of all MOF particles: (A) MOF-FA, (B) MOF-GA, (C) MOF-His, (D) MOF-BA, (E) MOF-TFA and (F) MOF-Li_2SO_4.

Table S1: Average size of all MOFs calculated after ImageJ analysis. 30 samples were measured per MOF.

	Number	**Average size (nm)**	**Variance**
MOF-BA	30	362.7	2132.1
MOF-FA	30	346.6	1080.2
MOF-GA	30	352.1	813.32
MOF-His	30	355.5	1786.3
MOF-Li_2SO_4	30	336.7	1131.8
MOF-TFA	30	347.8	914.24

Table S2: ANOVA analysis of the MOF particle sizes. As the p-value is larger than the significance level (0.05), no statistically significant difference in size exists between the samples.

ANOVA

Source of Variation	**SS**	**df**	**MS**	**F**	**p-value**	**F crit**
Between Groups	11680.1	5	2336	1.7837	0.1185	2.2661
Within Groups	227882	174	1310			
Total	239562	179				

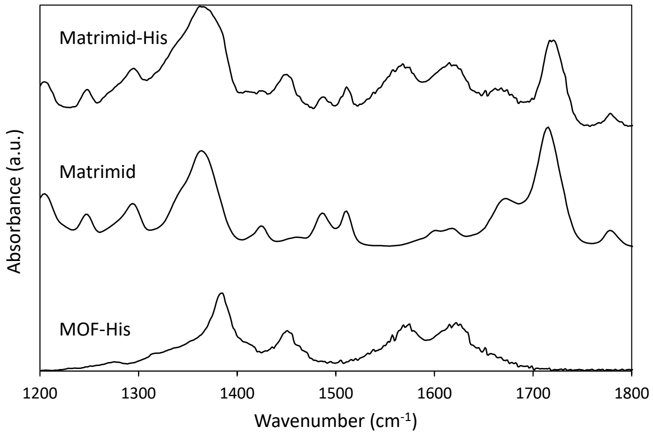

Figure S3~~3~~: ATR-FTIR spectrum of MMM-His, Matrimid and MOF-His.

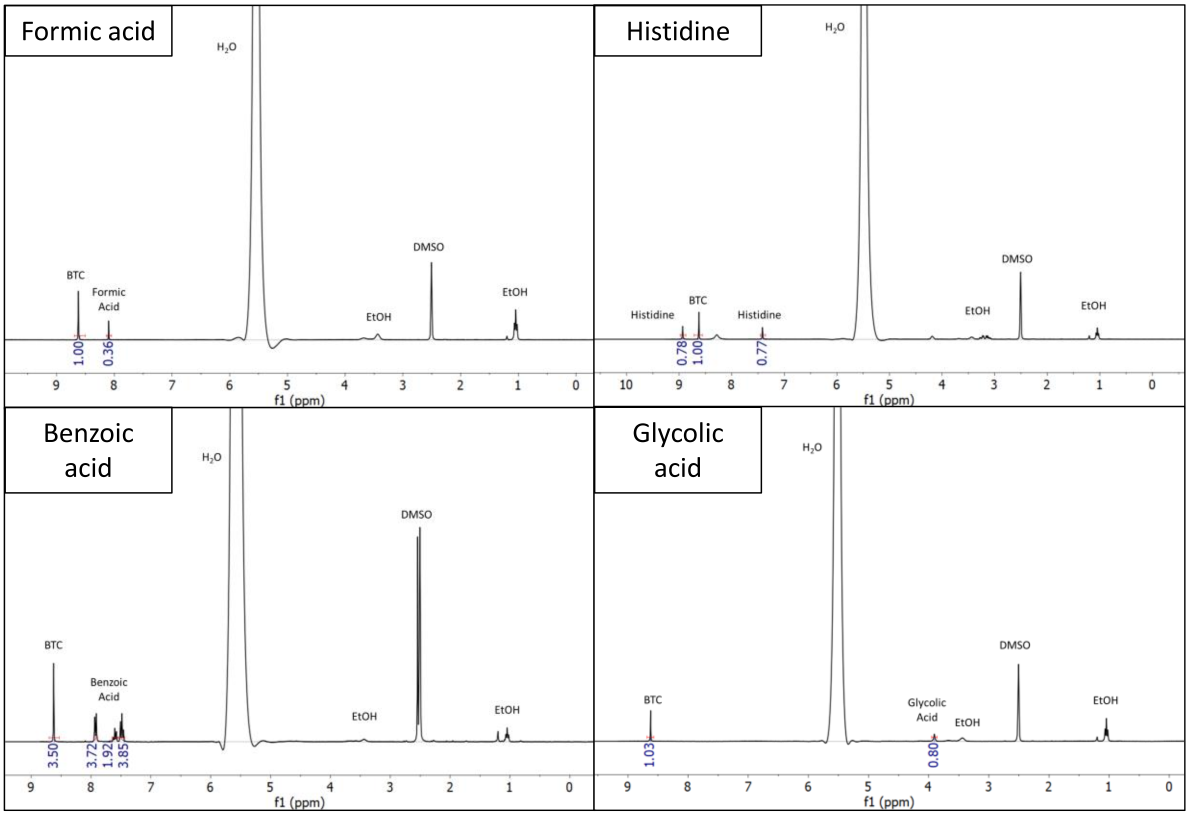

Figure S4: ^{1}H-NMR spectra for MOF-FA, MOF-BA, MOF-His and MOF-GA.

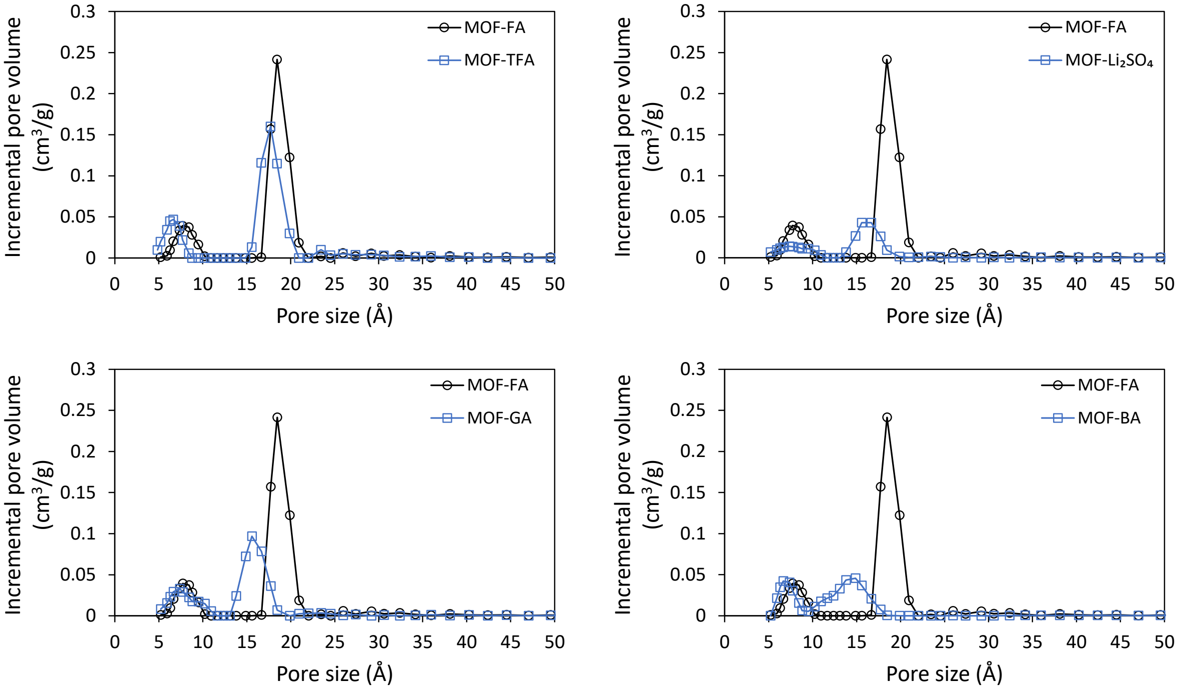

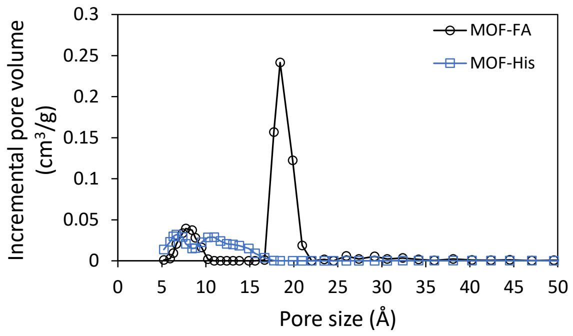

Figure S5: Incremental pore volume as a function of pore size for all MOFs.

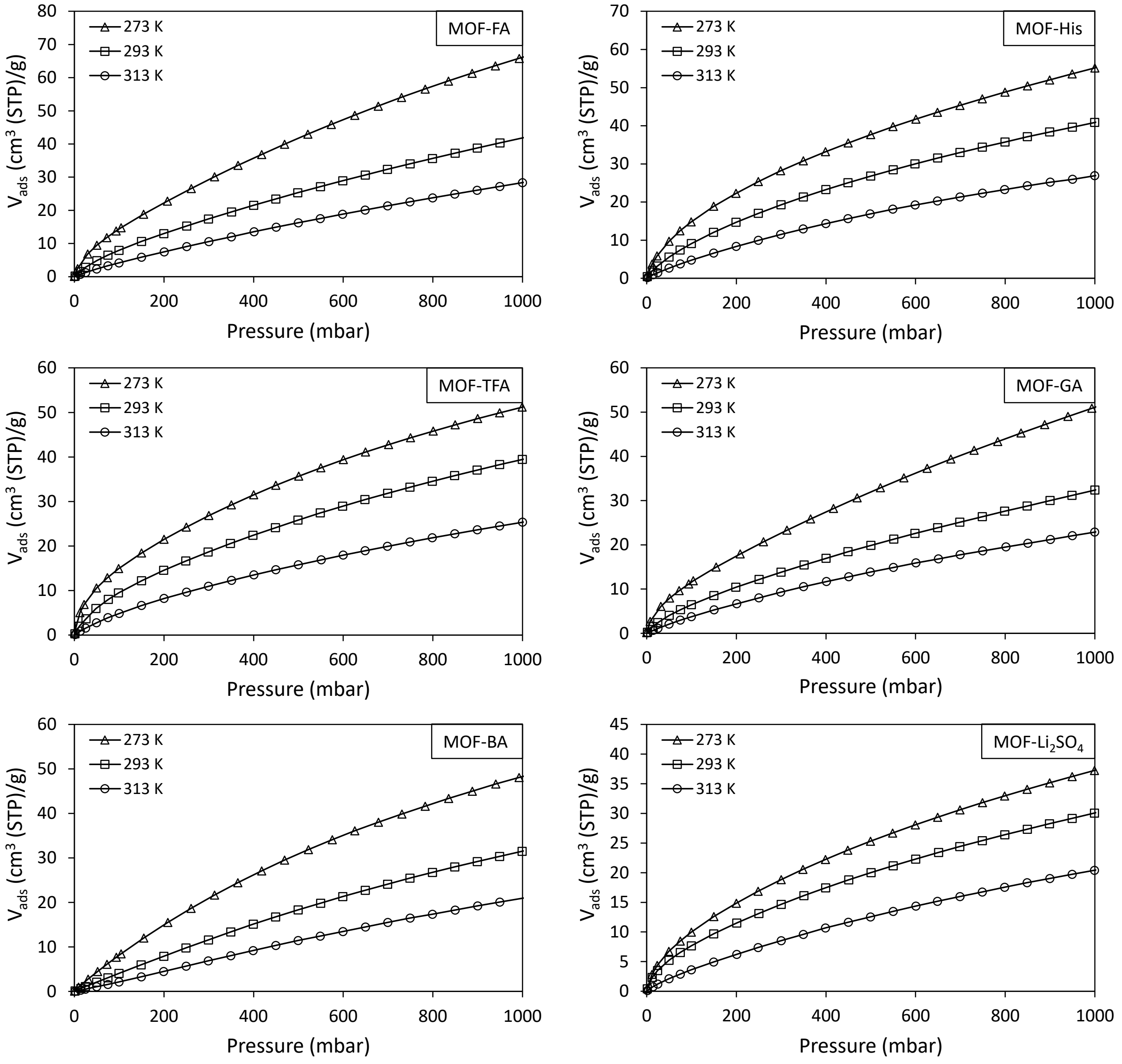

Figure S6: CO_2 uptake of all MOFs at 273 K, 293 K and 313 K.

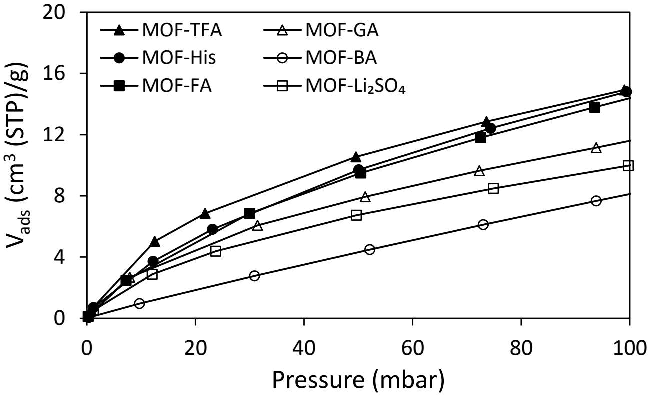

Figure S7: CO_2 adsorption isotherms of all MOFs in the low-pressure region (0-100 mbar) at 273 K.

Table S3: Model parameters for the dual-site Langmuir fit on the CO_2 adsorption isotherm at 273 K. N is the amount of adsorbed gas (cm^3 (STP)/g), $N_{m,A}$ and $N_{m,B}$ the amount of adsorbed gas at saturation for sorption site A and B, respectively (cm^3 (STP)/g) and b_A and b_B the adsorption equilibrium constants for, respectively, sorption site A and B. R^2 is the correlation coefficient.

	$N_{m,A}$	$N_{m,B}$	b_A	b_B	R^2
MOF-FA	0.34	8.74	0.046	0.00042	1.0000
MOF-GA	0.32	8.14	0.048	0.00031	1.0000
MOF-BA	0.04	4.95	0.014	0.00073	1.0000
MOF-TFA	0.43	4.44	0.056	0.00070	1.0000
MOF-His	0.59	5.59	0.020	0.00050	0.9999
MOF-Li_2SO_4	0.35	3.87	0.028	0.00051	0.9999

Table S4: CO_2 Q_{st} (kJ/mol) of all MOFs for different CO_2 loadings (0, 5, 15, 30 cm^3 (STP)/g).

	CO_2 adsorbed (cm^3 (STP)/g)			
	0	**5**	**15**	**30**
MOF-FA	30.9	34.1	25.6	22.1
MOF-His	31.8	30.1	25.6	22.4
MOF-TFA	39.2	37.2	27.7	22.5
MOF-GA	37.6	32.9	22.6	21.4
MOF-BA	23.9	22.8	21.8	20.7
MOF-Li_2SO_4	28.2	28.0	20.3	18.3

Table S5: Solubility (S) of CO_2 and N_2 in the Matrimid reference membrane and the MMMs. S_{CO2}/S_{N2} constitutes the CO_2/N_2 solubility selectivity. Measurements were conducted at 30 °C and varying pressures (see table).

Pressure (bar)	**Membrane**	**S_{N2}**	**S_{CO2}**	**S_{CO2}/S_{N2}**
5	Matrimid	0.00703	0.08125	11.6
	MMM-GA	0.00788	0.09487	12.0
	MMM-His	0.00809	0.10152	12.5
	MMM-FA	0.00694	0.10454	15.1
	MMM-BA	0.00578	0.10036	17.4
	MMM-TFA	0.00609	0.10828	17.8
	MMM-Li_2SO_4	0.00592	0.10901	18.4
10	Matrimid	0.00594	0.05615	9.45
	MMM-GA	0.00675	0.06699	9.92
	MMM-His	0.00692	0.06833	9.87
	MMM-FA	0.00586	0.07399	12.6
	MMM-BA	0.00571	0.06989	12.2
	MMM-TFA	0.00524	0.07603	14.5
	MMM-Li_2SO_4	0.00536	0.07594	14.2
15	Matrimid	0.00537	0.04539	8.46
	MMM-GA	0.00637	0.05398	8.46
	MMM-His	0.00611	0.05410	8.85
	MMM-FA	0.00515	0.06053	11.8
	MMM-BA	0.00529	0.05572	10.5
	MMM-TFA	0.00454	0.06277	13.8
	MMM-Li_2SO_4	0.00472	0.06062	12.9

Force fields

To perform static GCMC (Grand Canonical Monte Carlo) simulations for the differently functionalized MOF-808 structures, each structure was parametrized by a non-covalent force field that contains both electrostatic and van der Waals interactions:

$$V = V_{ei} + V_{vdW} \qquad \text{(Equation 8)}$$

The electrostatic interactions are modelled by a Coulomb interaction between Gaussian charge distributions, which are derived from cluster models of the MOF-808 $Zr_6O_8H_x$ brick, using phenyl terminations at the positions of the six BTC^{3-} linkers (Figure S8). After a geometry optimization with Gaussian 16[82], using the B3LYP functional[83] and 6-311g(d,p) basis sets[84] for all atoms but zirconium, for which the LanL2DZ basis set and pseudopotential are used[85], the electron density of the cluster is determined with gpaw[86] using the PBE functional[33]. Finally, the atomic charges q_i are derived with the Minimal Basis Iterative Stockholder (MBIS) partitioning scheme[87], so that the electrostatic interaction is given by

$$V_{ei} = \frac{1}{2}\sum_{\substack{i,j=1\\(i\neq j)}} \frac{q_i q_j}{4\pi\epsilon_0 r_{ij}} \operatorname{erf}\left(\frac{r_{ij}}{d_{ij}}\right) \qquad \text{(Equation 9)}$$

with r_{ij} the distance between atoms i and j, and q_i and d_i respectively the total charge and the radius of the Gaussian charge distribution[88] centered on atom i. The mixed radius d_{ij} of the Gaussian charges is given by $\sqrt{d_i^2 + d_j^2}$.

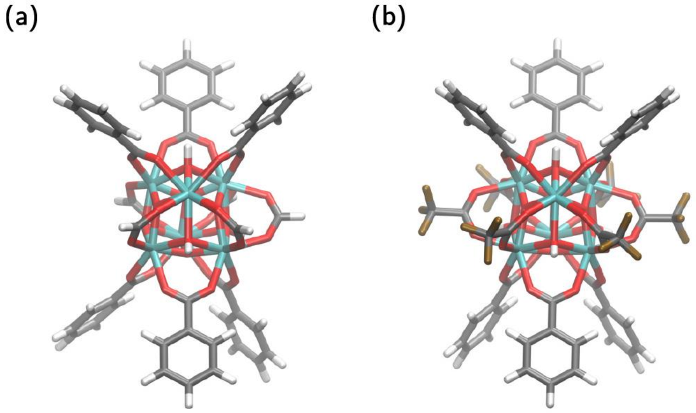

Figure S8: Cluster models used in the derivation of the atomic charges of (a) MOF-FA-def1 and (b) MOF-TFA.

The van der Waals interactions are modelled by a Lennard-Jones potential:

$$V_{vdW} = \sum_{i<j} 4\epsilon_{ij}\left[\left(\frac{\sigma_{ij}}{r_{ij}}\right)^{12} - \left(\frac{\sigma_{ij}}{r_{ij}}\right)^{6}\right] \qquad \text{(Equation 10)}$$

for which the parameters σ_{ij} and ϵ_{ij} between atom i and j are derived from the atomic DREIDING parameters[41] (and UFF parameters[43] for zirconium), using the Lorentz-Berthelot mixing rules:

$$\sigma_{ij} = \frac{\sigma_i + \sigma_j}{2} \text{ and } \epsilon_{ij} = \sqrt{\epsilon_i \epsilon_j} \qquad \text{(Equation 11)}$$

In the GCMC simulations, the Lennard-Jones interactions are truncated at 10.1 Å and complemented by the appropriate tail corrections.

Modelled CO_2 isotherms

The CO_2 adsorption isotherms obtained from GCMC simulations at different pressures for MOF-FA and MOF-TFA are given in Figure S9. The isotherms for both MOF-FA and MOF-TFA are similar to the experimental ones, although small differences can be observed. These can be attributed to the different number of modulator molecules on the zirconium cluster and the slightly higher temperature at which CO_2 adsorption was simulated. For MOF-FA, two defect structures with, respectively, one and three missing formate groups per zirconium cluster are modelled next to the pristine MOF-FA (containing six formate groups per cluster). The absolute differences (i.e. the number of adsorbed CO_2 molecules per unit cell) between the pristine and defects structures are small and only significant at higher pressures. However, per unit of mass, this results in a slightly larger uptake for MOF-FA with three defects in comparison to pristine MOF-FA.

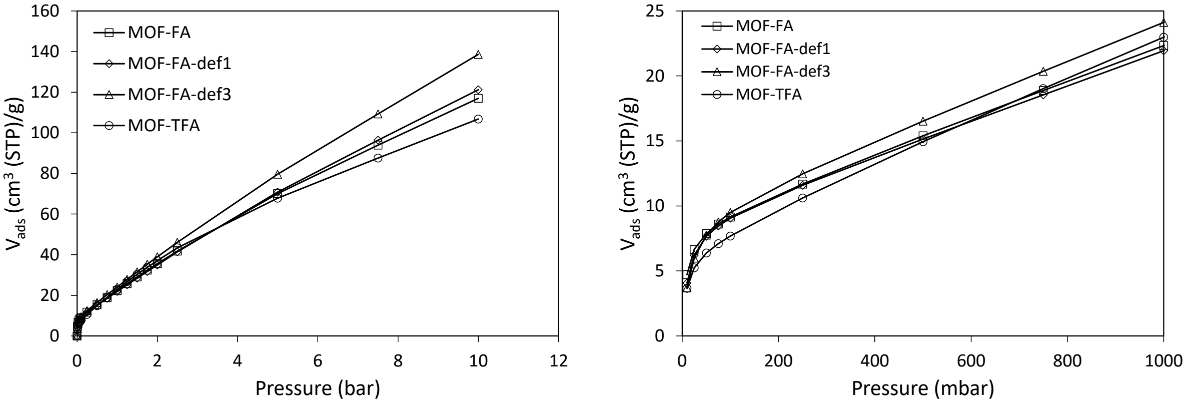

Figure S9: Modelled CO_2 adsorption isotherms for MOF-FA and MOF-TFA. For MOF-FA, the number of defects (i.e. absence of formate molecule) on the zirconium clusters has been varied from one (MOF-FA-def1) to three (MOF-FA-def3).

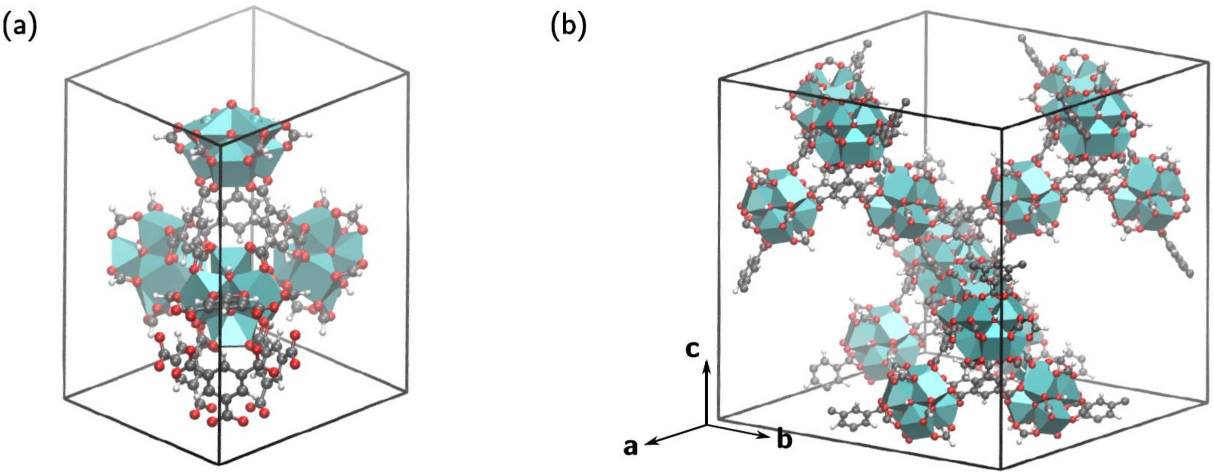

Figure S10: (a) Primitive unit cell of MOF-FA. (b) Conventional cubic unit cell of MOF-FA.

The CO_2 density in MOF-FA-def1 exhibits only small differences in comparison with the pristine MOF-FA. MOF-FA-def3, on the other hand, does show some interesting differences (Figure S11). Similar to MOF-FA, the CO_2 molecules are first adsorbed in the cages of the linkers, yielding a square grid of adsorption sites when viewing MOF-808 along the c-axis. The second type of adsorption sites, covering the open sides of the linkers, become more prominently occupied with increasing pressure, but do not longer give rise to a square grid of adsorption sites. This is due to the fact that an additional type of adsorption sites is present in MOF-FA-def3, located on the open metal sites of the zirconium clusters (marked as site 3 in Figure S11). These adsorption sites are observed to be more favorable than the adsorption sites located at the linkers. With increasing pressure the MOF-808 structure exhibits a different encapsulation, which is primarily formed by the adsorption sites at the open metal sites and the adsorption sites at the open sides of the linkers. The adsorption sites above the benzene rings of the linkers are not as significantly occupied as in pristine MOF-FA, not even at the highest pressures.

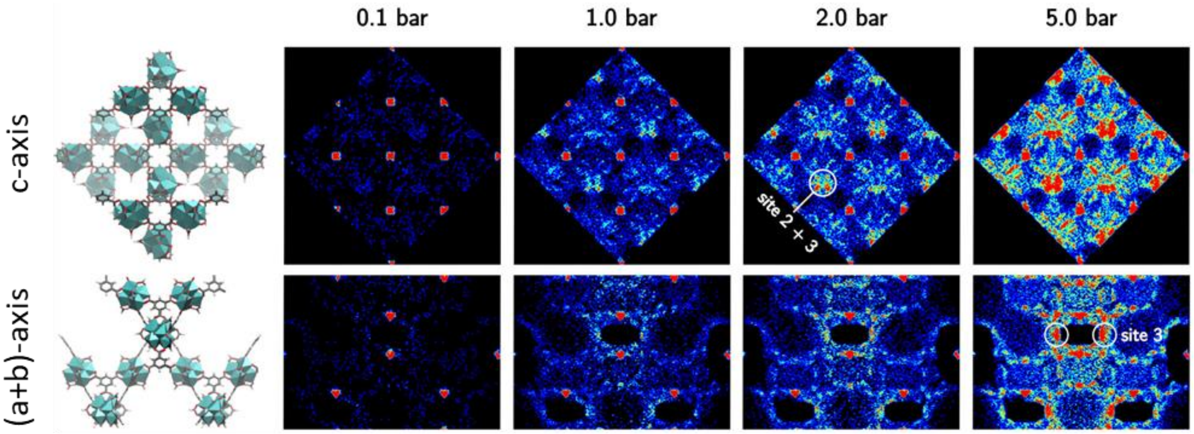

Figure S11: Density of the adsorbed CO_2 molecules in MOF-FA-def3 at 300 K projected on a plane orthogonal to the c-axis and the (a + b)-axis of the conventional unit cell. The CO_2 molecules are represented by the positions of the carbon atoms.

Table S6: Simulated adsorption enthalpies for MOF-FA, MOF-TFA and MOF-FA with 1 and 3 defect(s), respectively.

Pressure (bar)	MOF-FA	MOF-FA-def1	MOF-FA-def3	MOF-TFA
0.010	-45.2	-43.7	-41.2	-44.8
0.025	-41.6	-41.2	-39.2	-40.6
0.050	-35.2	-36.2	-35.3	-34.3
0.075	-30.1	-31.8	-31.7	-30.3
0.10	-26.8	-28.5	-28.8	-27.9
0.25	-20.5	-21.0	-21.5	-23.9
0.50	-19.1	-19.0	-19.4	-23.1
0.75	-18.7	-18.6	-18.9	-22.9
1.00	-18.6	-18.4	-18.7	-22.8
1.25	-18.4	-18.3	-18.6	-22.7
1.50	-18.4	-18.2	-18.5	-22.6
1.75	-18.3	-18.2	-18.4	-22.5
2.00	-18.2	-18.1	-18.4	-22.4
2.50	-18.1	-18.0	-18.3	-22.1
5.00	-17.4	-17.5	-17.9	-20.7
7.50	-16.9	-17.0	-17.5	-19.4
10.0	-16.5	-16.6	-17.1	-18.6

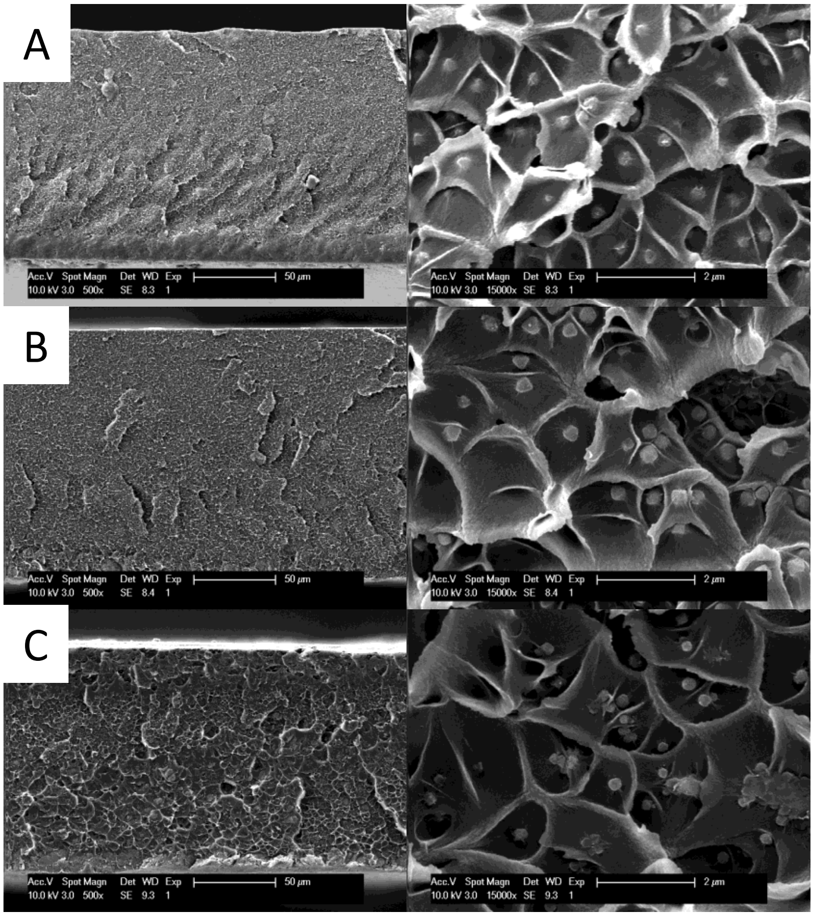

Figure S12: SEM cross-sections of A) MMM-FA, B) MMM-BA and C) MMM-TFA. All MMMs contain 10 wt.% MOF.

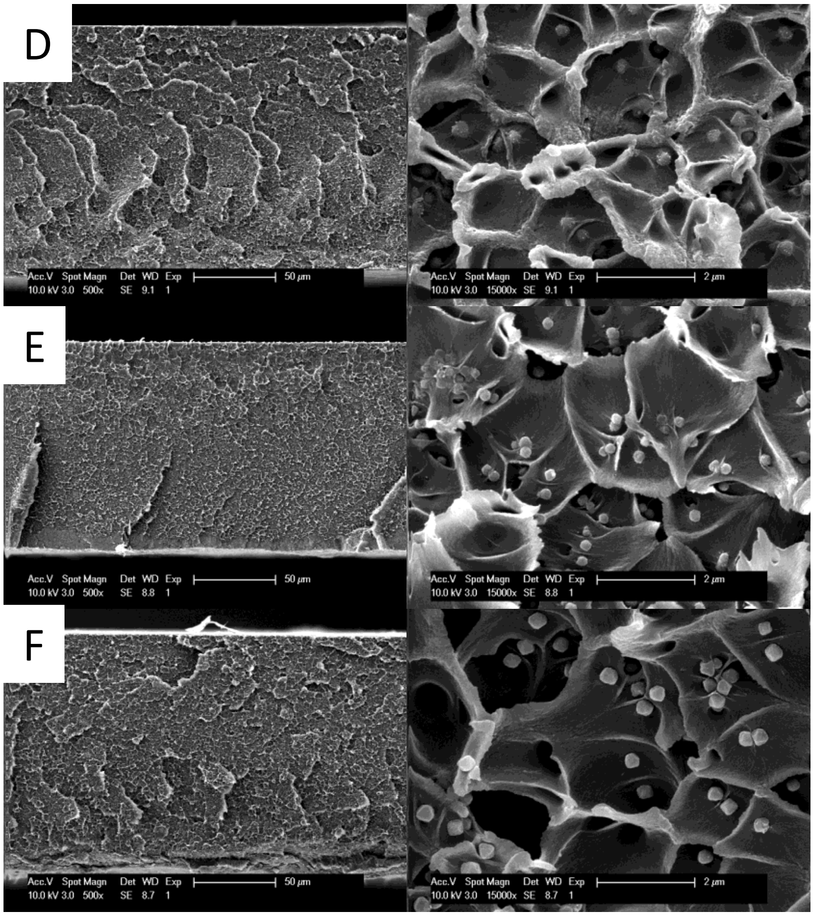

Figure S13: SEM cross-sections of D) MMM-GA, E) MMM-His and F) MMM-Li_2SO_4. All MMMs contain 10 wt.% MOF.

Table S7: Thermal analysis of all membranes.

	Glass transition temperature (T_g, °C)	**Decomposition temperature (T_d, °C)**	**Weight % MOF according to TGA**
Matrimid	312	555	-
MMM-FA	324	548	10
MMM-GA	320	547	9
MMM-BA	322	550	8
MMM-His	322	553	8
MMM-TFA	320	552	8
MMM-Li_2SO_4	322	-	-

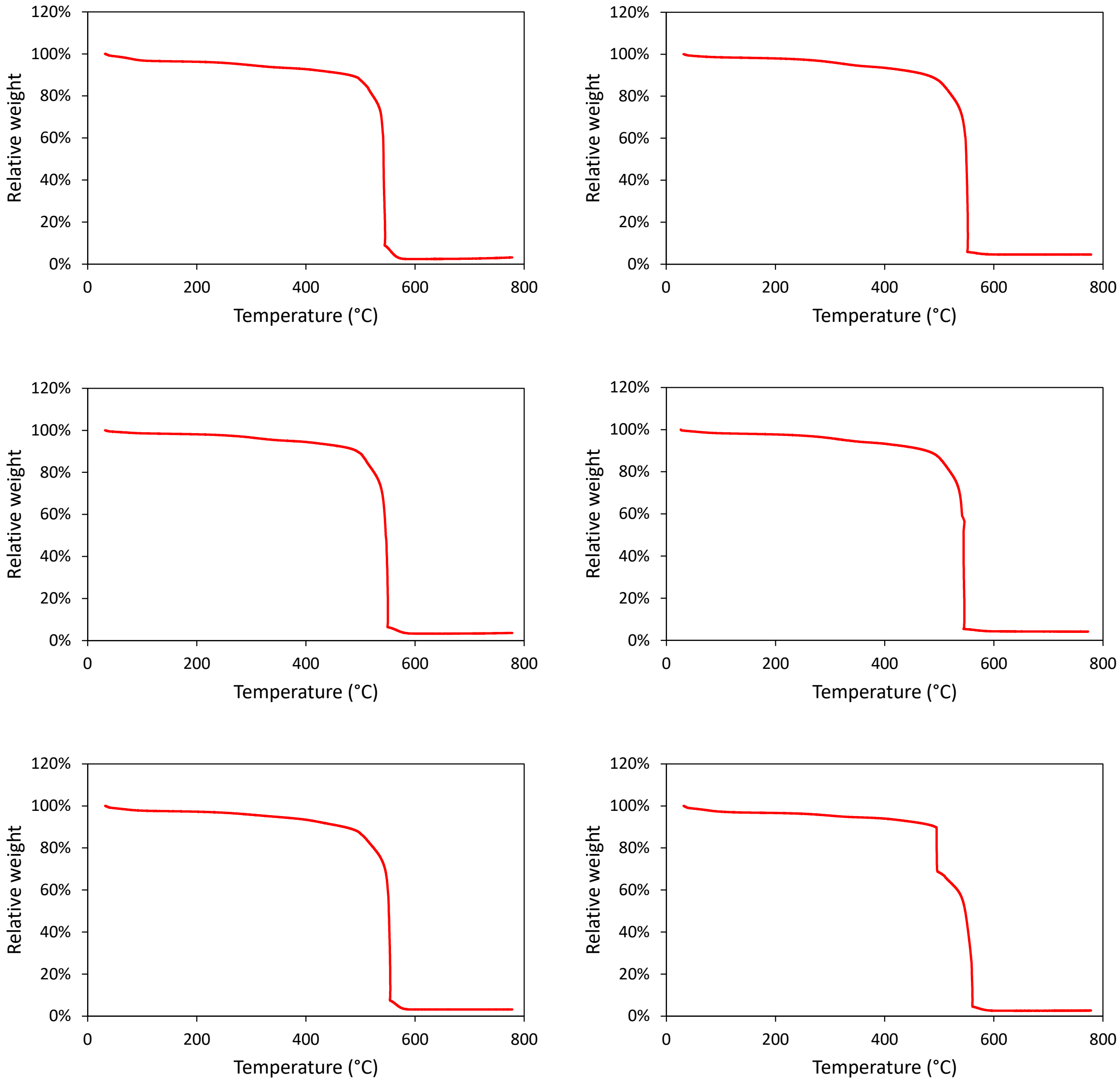

Figure S14: TGA traces of MMM-FA (top left), MMM-TFA (top right), MMM-BA (middle left), MMM-GA (middle right), MMM-His (bottom left) and MMM-Li_2SO_4 (bottom right).

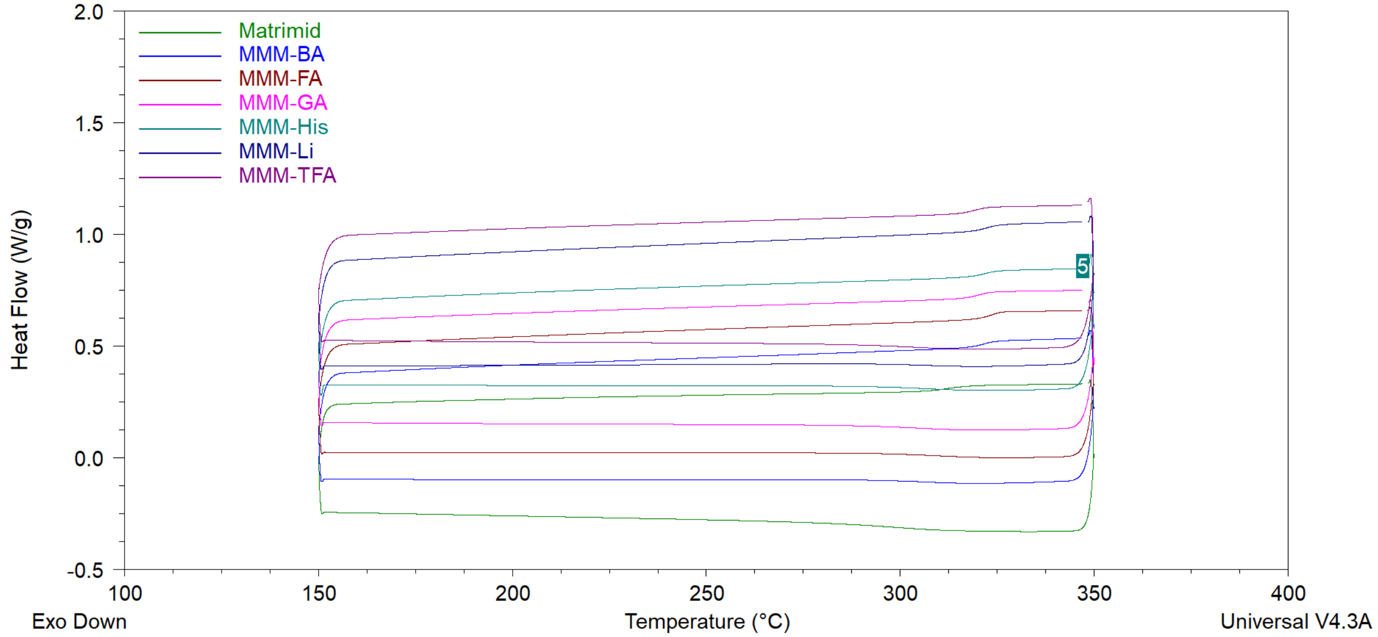

Figure S15: DSC traces of all MMMs and Matrimid.

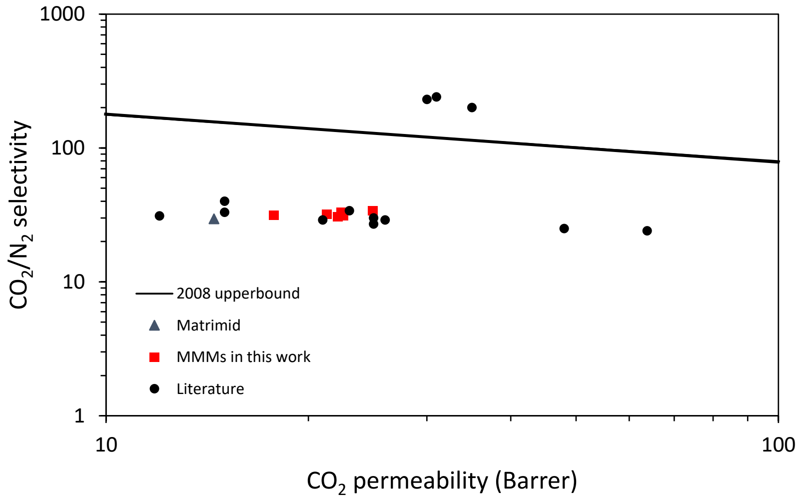

Figure S16: Comparison of the performance of the MMMs produced in this work with literature[76,89–92] and the 2008 Robeson CO_2/N_2 upper bound.

Table S8: Correlation factors between MOF parameters.

		273 K		293 K		313 K						
	Correlation of MOF parameters	CO_2 uptake (50 mbar)	CO_2 uptake (1000 mbar)	CO_2 uptake (50 mbar)	CO_2 uptake (1000 mbar)	CO_2 uptake (50 mbar)	CO_2 uptake (1000 mbar)	BET surface area	Pore volume	$Q_{st,0}$	$Q_{st,15}$	$Q_{st,30}$
273 K	CO_2 uptake (50 mbar)	1.00	0.22	0.85	0.81	0.95	0.78	0.54	0.50	0.77	0.86	0.67
	CO_2 uptake (1000 mbar)		1.00	-0.25	0.63	-0.09	0.70	0.82	0.83	0.03	0.53	0.66
293 K	CO_2 uptake (50 mbar)			1.00	0.51	0.96	0.44	0.17	0.10	0.61	0.54	0.21
	CO_2 uptake (1000 mbar)				1.00	0.64	0.98	0.64	0.61	0.36	0.92	0.83
313 K	CO_2 uptake (50 mbar)					1.00	0.59	0.29	0.24	0.73	0.69	0.43
	CO_2 uptake (1000 mbar)						1.00	0.69	0.66	0.36	0.85	0.81
	BET surface area							1.00	0.99	0.45	0.67	0.61
	Pore volume								1.00	0.48	0.67	0.67
	$Q_{st,0}$									1.00	0.59	0.53
	$Q_{st,15}$										1.00	0.90
	$Q_{st,30}$											1.00

Table S9: Correlation factors between membrane parameters.

Correlation of membrane parameters	$\alpha_{15/85}$	$\alpha_{50/50}$	α_{ideal}	$P_{15/85}$	$P_{50/50}$	$P_{100/0}$	CO_2 uptake (1 bar)	CO_2 uptake (2 bar)	CO_2 uptake (3 bar)	CO_2 uptake (4 bar)	CO_2 uptake (5 bar)
$\alpha_{15/85}$	1.00	0.89	-0.97	0.58	0.74	0.55	0.42	0.36	0.38	0.41	0.39
$\alpha_{50/50}$		1.00	-0.80	0.73	0.75	0.74	0.03	-0.05	-0.04	-0.01	-0.03
α_{ideal}			1.00	-0.39	-0.59	-0.37	-0.56	-0.49	-0.49	-0.52	-0.47
$P_{15/85}$				1.00	0.95	0.98	-0.18	-0.21	-0.20	-0.20	-0.16
$P_{50/50}$					1.00	0.90	0.14	0.11	0.11	0.10	0.13
$P_{100/0}$						1.00	-0.27	-0.33	-0.33	-0.34	-0.31
CO_2 uptake (1 bar)							1.00	0.98	0.95	0.92	0.87
CO_2 uptake (2 bar)								1.00	0.99	0.97	0.94
CO_2 uptake (3 bar)									1.00	1.00	0.98
CO_2 uptake (4 bar)										1.00	0.99
CO_2 uptake (5 bar)											1.00